

INFLUENCE OF ADDITIVE MANUFACTURING PROCESS
PARAMETERS ON SELECTIVE LASER MELTING OF CL-
91RW HOT-WORKING STAINLESS STEELS

by

Mackenzie Purdy

B.Sc., University of New Brunswick, 2018

A Thesis Submitted in Partial Fulfilment of
the Requirements for the Degree of

Master of Science

in the Graduate Academic Unit of

Mechanical Engineering

Supervisor(s): Mohsen Mohammadi, PhD, Mechanical Engineering

Examining Board: Andy Simoneau, PhD, Mechanical Engineering, Chair
Clodualdo Aranas, PhD, Mechanical Engineering
Eric Hildebrand, PhD, Civil Engineering

This thesis is accepted by the
Dean of Graduate Studies

THE UNIVERSITY OF NEW BRUNSWICK

March, 2022

© Mackenzie Purdy, 2022

Abstract

In this thesis, the commissioning of a manufacturing metal 3D printer (Concept Laser M2) was undertaken. Commissioning of metal 3D printing requires an experimental approach. Materials manufactured in this fashion behave differently depending on both hardware factors such as laser power, speed, spot size, and environmental factors such as inert gas utilized (argon or nitrogen), calibration, auxiliary condition, and powder quality.

A knowledge foundation including CAD preparation, employing parameter sets, print setup, and powder removal was developed. Several geometries were printed by employing parameters for CL-50WS (MS-1), CL-20ES (316L), and CL-91RW alloys. A preliminary study of laser power and speed and the effects on the porosity and melt pool morphology of additively manufactured CL50WS (MS-1) maraging steel were studied. This revealed the effects of processing parameters on the physical properties of the samples printed and explored some limitations of the machine.

Forty cubic samples of CL-91RW were generated varying laser power and speed from 270 to 326 watts, and 900-1100 mm/s respectively. Sample density was determined using the Archimedes method and showed a density within 5% of the maximum, with the densest sample being 6.324 g/cm³.

Dedication

This thesis is dedicated to my parents and girlfriend for their warm spirits that motivated me throughout this process.

Acknowledgement

I am grateful to Dr. Mohsen Mohammadi, who gave me this opportunity to start my journey as an M.Sc. student and guided me through this process. Through the M.Sc. I learned how to broaden my vision, and to explore all existing capabilities to complete a task.

I want to thank Dr. Clodualdo Aranas for keeping me focused and checking in on my work, and being open to collaboration, and Dr. Andy Simoneau, and Dr. Tiger Jeans who stand on the committee.

I am grateful to the Mechanical Engineering department staff who provided support for me during this time at UNB, Paulette Steever, Ann Bye, and Debbie Basque. I am of course thankful to other members including the technicians who helped me conduct the experiments, Vince Boardman, and Brian Guidry.

I am thankful for the support from my colleagues at the Marine Additive Manufacturing Center of Excellence (MAMCE).

I should thank my parents, Derek and Marge Purdy, and brother Frank Purdy who always support me and are available whenever I need them.

Finally, I need to thank my girlfriend Victoria Forbes for being so patient and supportive. To you, I owe a great deal of thanks.

Table of Contents

Abstract	ii
Dedication	iii
Acknowledgement	iv
Table of Contents	v
List of tables.....	vii
List of figures.....	viii
Chapter 1 Introduction	1
1.1 Maraging steels	3
1.2 Additive manufacturing	4
1.3 Literature review	6
Additive Manufacturing processes.....	6
1.3.1 Powder Production.....	11
1.3.1.1 Gas Atomization	11
1.3.1.2 Mechanical Milling	12
1.3.1.3 Water Atomization.....	13
1.3.1.4 Energy density and optimization of process parameters.....	15
1.3.1.5 Process Induced Defects	20
1.3.2 Maraging Steels, 17-4 PH Steels, and CORRAX™	24
M	26
C	26
Chapter 2 Experimental Method.....	27
2.1 Experimental procedures	27
2.1.1 Commissioning of a Laser Powder Bed System.....	27
2.1.2 Materials and LPBF process	30
2.1.3 Characterization	32
Chapter 3.....	34
3.1 Operational knowledge of the machine	35
3.1.1 Pre-print Processing	35
3.1.2 Print Set-up	37
Chapter 4.....	42
4.1 Results.....	42

4.1.1 Commissioning	42
4.1.1.1 Magics STL development	42
4.1.1.2 Part and parameter development.....	43
4.1.2 Density Analysis	48
4.1.3 Energy Density.....	51
4.2 Discussion.....	52
Chapter 5 Future works and final remarks.....	58
5.1 Recommendation for future work	58
5.1.1 Exploration of Mechanical Properties and Microstructure	58
5.1.2 Modelling and simulations.....	59
5.2 Conclusions.....	60
References.....	61
Curriculum Vitae	

List of tables

Table 2-1 Chemical composition of maraging steel MS1 powder ([83])	31
Table 2-2 LPBF process parameters applied in this research	31
Table 4-1 Sample density and weight in air and water	49
Table 4-2 Melt pool width for 950 mm/s scan speed.....	55

List of figures

Fig. 1-1 Laser Powder Bed Fusion (LPBF) [12].....	3
Fig. 1-2 a) Selective laser sintered surface, b) Selective laser melted surface [18]	7
Fig. 1-3 Schematics showing the two principal methods of material delivery in DED for functionally graded material creation: (a) Coaxial multiple powder delivery (b) Wire and powder side fed delivery [24].	9
Fig. 1-4 (a) Schematic diagram of plasma deposition showing the position of the wire relative to the heat source and deposit; (b) a typical frame indicating the points of interest: nozzle position (N1 and N2), the wire reference mark (WR), the previous layer (y_p), current layer (y_c), wire fusion line (y_f), and top of the melt pool (y_m) [32].	10
Fig. 1-5 Gas atomization process schematic: a) Free fall gas atomization, b) The process of close-coupled gas atomization [41]	12
Fig. 1-6 SEM images of the as-received powder and the powders that were mechanically milled for various treatment periods; (a) as-received, (b) milled for 5 h, (c) milled for 10 h, and (d) milled for 20 h [35]	13
Fig. 1-7 Water atomization process [41].....	14
Fig. 1-8 Water atomized powder morphology [39]	14
Fig. 1-9 Laser power vs. Volumetric Energy Density in J/mm^3 and the resultant density [47] ..	16
Fig. 1-10 Assessment of laser power and scan speed influence on microstructural features and consolidation of AISI H13 tool steel processed by additive manufacturing [50]	17
Fig. 1-11 Comparison of geometrical and mechanical properties curves of different processing parameters between the experimental results, empirical formulas, and analytical prediction: a) relative density, b) yield stress [51]	18
Fig. 1-12 Results from in situ tensile tests. Engineering stress versus reduction of area for the wrought versus as built and the wrought versus annealed samples [53].....	19
Fig. 1-13 Representative examples of cross-sectional melt pool morphologies. (a) desirable, (b) balling, (c) under-melting, (d) severe keyholing, and (e) keyholing porosity [57].....	21
Fig. 1-14 Balling defect under SEM [61]	22
Fig. 1-15 Top surfaces characterization of EBM samples versus line offset (all images are the same magnification). (a) 0.10 mm. (b) 0.14 mm. (c) 0.18 mm. (d) 0.22 mm. (e) 0.26 mm. (f) 0.30 mm. [55].....	23
Fig. 1-16 Keyhole melt pool with trapped gas pore [78]	24

Fig. 1-17 (a, b) Optical microscopy images (a) 170 W and 2500 mm s ⁻¹ and (b) 230 W and 1667 mm s ⁻¹ ; (c) change in melt pool depth as a function of volumetric energy density [81].	25
Fig. 1-18 Columnar and cellular structure present in Corrax® [78].	26
Fig. 2-1 Contour, core, and downside surface elements	28
Fig. 2-2 Surface patterns a) continuous b) islands	29
Fig. 2-3 Archimedes Apparatus	33
Fig. 3-1 Fixing STL Files.	36
Fig. 3-2 Handling station with gloved door	37
Fig. 3-3 Build plate bolt pattern.	38
Fig. 3-4 Master recoater blade second zero check	39
Fig. 3-5 Recoater blade install	40
Fig. 3-6 Knurl locations for adjustment	40
Fig. 4-1 Test plate maraging steel.	43
Fig. 4-2 Maraging steel failed test print piece	44
Fig. 4-3 Hybrid injection molding die. Welding seam identified.	45
Fig. 4-4 316L print: a) full build, b) Unsupported outer surface failure (45-degree impeller), c) Unsupported hole failure (70-degree impeller).	46
Fig. 4-5 Forty CL-91RW sample printed using varying parameters	47
Fig. 4-6 Zoomed in samples 6, 16, 26 and 36. Surface roughness can be visually compared.	47
Fig. 4-7 CL-91RW sample print	48
Fig. 4-8 Laser Power vs Theoretical density.	50
Fig. 4-9 Laser speed vs Theoretical density.	51
Fig. 4-10 OM images of melt pools with Laser speed of 900mm/s and laser powers as follows: a) 270W, b) 286W, c) 302W, d) 318W. The scale is set to 50 microns.	54
Fig. 4-11 OM images of melt pools with Laser speed of 950mm/s and laser powers as follows: a) 270W, b) 278W, c) 294W, d) 318W. The scale is set to 50 microns.	55
Fig. 4-12 OM images of melt pools with Laser speed of 1000 mm/s and laser powers as follows: a) 270W, b) 278W, c) 302W, d) 326W. The scale is set to 50 microns.	56

Chapter 1

Introduction

The current gross domestic product (GDP) of Canada's manufacturing industry amounts to \$174 billion dollars, representing 10% of the total GDP [1]. Additive manufacturing (AM) has the potential to achieve 1% of the countries GDP in the next 5 years [2]. In addition to the projected increase in GDP, additive manufacturing is predicted to decrease energy consumption in manufacturing and reduce waste products [3, 4].

Additive Manufacturing offers a new technique to produce materials that allows for increased design complexity, yields stronger, more lightweight, and load specific components, as well as allow for the potential to perform on-site repairs eliminating the need for outsourcing components critical to an industrial operation. AM is a layer-by-layer process, meaning, it is performed by adding layers of powder or wire and melting or sintering these layers together to produce a product [5]. Parts produced in this manner are typically computer generated starting with a CAD file and converting to an STL (Standard Tessellation Language) file which meshes the CAD into a series of triangles. STL files are sliced into a series of section views of a given layer thickness, the sliced files are then sent to the printer and the product is created.

A significant focus of research in AM has been directed toward optimizing print process parameters for the current materials list; however, the current state of AM is still in its infancy with respect to the vast material processing knowledge developed over centuries of more traditional methods such as casting and forging. Consistent developments are being made in many disciplines within additive manufacturing including build volume

expansion, materials development, laser types, power capabilities, and various other methods such as friction welding and cold spray technologies [6, 7, 8].

Processes like forging and casting have dominated the manufacturing field for centuries. AM offers a fresh and new perspective that has a greater degree of customization and offers unique, advanced solutions to some problems posed by the former technologies. Complex geometries, embedded systems, increased production speed, and decreased waste material are examples of some of the benefits that AM brings that are appealing to manufacturers and their customers [9].

AM is a complex process that can produce low quality components if the machine is not calibrated sufficiently. Calibration of the machine is important in all cases to minimize inconsistencies and produce successful components. Instances such as incorrectly installed recoaters, dirty laser windows, and non-level build plates can have detrimental effects on the product [10, 11]. Proper training and testing to facilitate competence and consistency between prints allows for industry confidence in the components.

Steels have been of focus in AM recently due to their superior mechanical properties and versatility when produced using this method. Steels such as maraging and certain hot working steels are iron-based alloys with low carbon content and higher Ni contents, providing an affinity for the AM process as the higher temperature gradients present during this process. The material discussed in this research is known as stainless hot-working steel, containing 12% Cr and 9.2 % Ni.

The primary method of AM used for this study is known as the Laser Powder Bed

Method (LPBF) or Selective Laser Melting (SLM). This method, as seen in Fig. 1-1 consists of a powder chamber, build platform and powder collection container. In addition to the Ytterbium doped fibre laser and recoater.

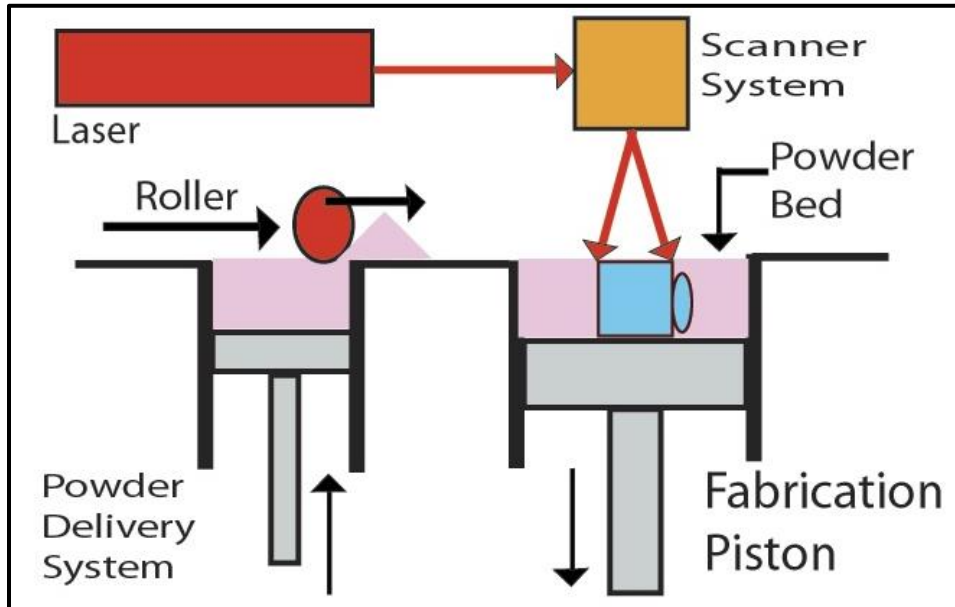


Fig. 1-1 Laser Powder Bed Fusion (LPBF) [12]

1.1 Maraging steels

Maraging steel high-strength steel class was first introduced and developed during the 1950's and is of great importance today. This alloy consists of high nickel content with a low carbon weight percentage. The martensitic (bcc) structure is formed during a diffusionless transformation from (fcc) crystal structure in maraging steels. The name maraging is based on the aging of martensitic structure in these alloys; see, e.g. (Floreen, 1968), (Sha, et al., 1993), (Belyakov, et al., 1968) for more details.

The three essential alloying elements in this type of material are nickel, cobalt, and molybdenum, followed by titanium and aluminum. Each alloying element has its effect on the material's behavior and changing the weight balance highly affects the microstructure

and mechanical properties. It is worth noting that, the maraging steel contains carbon lower than 0.03% (weight) and the intermetallic precipitates govern the age hardening.

Each alloying element has its footprint in maraging steel. The nickel has two major contributions to the mechanical properties, which are helping to form precipitates as well as controlling the austenite reversion. Although cobalt forms no precipitates, the cobalt element's existence prevents the formation of molybdenum solution in the matrix and results in the formation of Fe₇Mo₆ precipitates. As mentioned earlier, titanium and molybdenum form precipitations, which are the main strengthening mechanisms in maraging steel (Sha et al., 1993).

Many comprehensive studies have been conducted exploring the influence of process parameters on the production of maraging steels. Tan *et al.* explored the effects of build orientation on microstructure and mechanical properties, they recognized that laser parameters were crucial in the development of fully dense components. Laser speed and power represent the most prominent effect on the density of printed parts being the primary modes of laser modification [13]

1.2 Additive manufacturing

AM's three main processes are introduced using different machine manufacturers called sintering, melting, and metal deposition processes (Gu et al., 2012). Selective metal sintering (SMS) was one of the initial steps forward to make metal parts using additive procedures. In this method, heat applied to one metal powder layer melts the layer, and after solidification, a new layer is added the same way to the previous one, and this incrementally produces a 3D object, see e.g., (Van der Schueren et al., 1995), (Agarwala, et al., 1995), (Kruth et al., 1996). On the other hand, in the SLS process, the laser beam

acts as the heat source on the metal powder to make the 3D object (Kruth et al., 1998). The latter technique and the melting process were then called selective laser melting (SLM) or laser beam melting (LBM). An alternative for laser as the heat source has been the electron beam, which led to another technique parallel to SLM called electron beam melting (EBM) (Murr et al., 2012). EOS GmbH has introduced its own SLM technique called direct metal laser sintering (DMLS) which was the process used to produce all the samples for this study.

SLM is a product of complex phenomena including laser power and speed, gas type and flow speed, the distance between melt pools, layer thickness, etching strategy, and complex solidification behaviour that can be drastically influenced by the set-up of the printer. Commissioning and understanding of machine behaviour with the processing and modification of parameters is important to ensure repeatability between prints. Leo *et al.* found that defocusing of the laser with 17-4 PH resulted in differences in grain size and amount of austenite present [14]. These changes can be detrimental to the mechanical properties of the printed part and are influenced by improper pre-processing of the print and can be affected by misalignment of as little as 1mm. Before commissioning the printer, different additive techniques were studied to obtain a baseline understanding of variations of building designs and techniques.

1.3 Literature review

Additive Manufacturing processes

There are several types of metal AM processes each with their own advantages and disadvantages. These systems are primarily solid, powder, or liquid based. Each system presents its own unique set of challenges for manufacturing quality components. This necessitates an elaborate understanding of individual machine's capabilities and behaviours of the materials after parameter modifications.

Powder bed fusion (PBF), also known as laser powder bed fusion (LPBF), can be subdivided into two categories, Direct Metal Laser Sintering (DMLS) and Selective Laser Melting (SLM) [15, 16]. These processes utilize a powder deposit system that releases the metal powder outside, or along the edge of the build space. The powder is then evenly distributed along the build surface by a sweeper or brush. A pattern is etched into the surface using a CO₂ or Yb doped YAG fibre laser excited by a flash lamp or diode pump, the surface is melted using a scanning system [17, 18].

SLM depicts the complete melting of the material, where it limits the potential to develop inconsistencies such as pores in the material, as the metal powder is excited to just above melting temperature, and the molten metal fills all cavities created. SLM is usually used for homogenous materials, as the melting temperatures for alloys may vary with alloying elements. During SLM, process parameters must be adjusted to avoid potential defects from occurring because of phenomenon such as balling, keyholing and vaporization [19]. SLS differs from SLM in that it excites the powder to temperatures between $T_{melt}/2$ and T_{melt} . This process is called Solid State sintering. In this process, the molecular bonding

does not allow the powder to evenly melt. SLS is usually the preferred method when using alloys, as each component may have drastically different melting properties. Since the molten powder does not have time to distribute properly, the potential for pores to be created increases in SLS, which inhibits the performance of the components [20, 21, 22]. In cases such as biomedical, the increased porosity is necessary to achieve complete adhesion and promote the growth of bones and other components of the body [23].

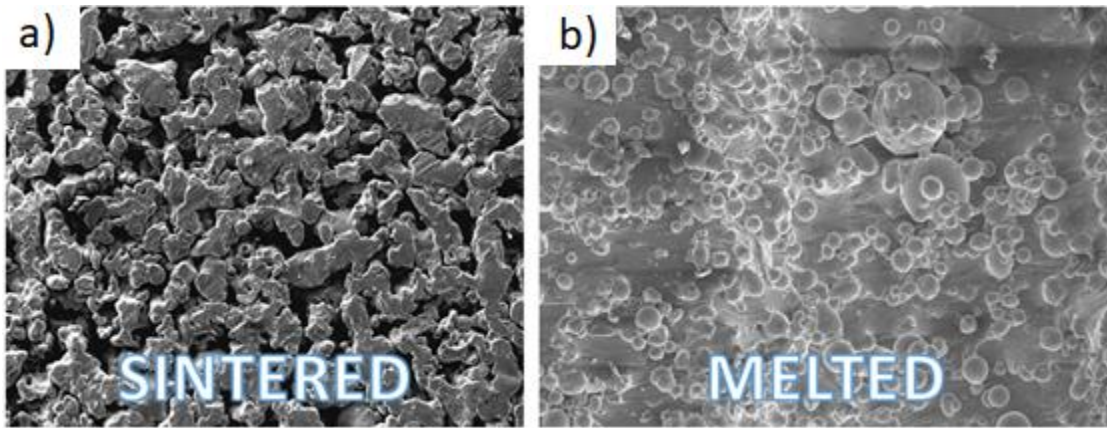


Fig. 1-2 a) Selective laser sintered surface, b) Selective laser melted surface [18]

Electron Beam melting (EBM) is a technique like SLM, however, there are several differences between them. EBM uses an electron gun, accelerated with a 4.5 kV potential, that is focused using electromagnetic lenses [24]. The electron beam is scanned across the surface in multiple passes at a user-supplied scan speed, with a high current pre-heating the powder to temperatures not achievable through the SLM process. The typical pre-heat temperature is eighty percent of the melting temperature. Once this temperature is achieved, the current and scan speed is reduced. Similar to the SLM process, the electron beam is applied to only the area described by the CAD software connected to the EBM machine. The final key difference is unlike SLM, which is operated in an inert environment usually consisting of argon or nitrogen, EBM operates in a vacuum. This environment

inhibits oxidation to a greater degree which is especially useful for materials such as titanium that react quite easily with oxygen. Small helium gas is applied to the vacuum to improve the heat transfer characteristics of the material [25].

Powder and wire feed techniques have most of the same components as their powder bed counterparts, however they offer much more flexibility with part design. These techniques utilize a powder/wire delivery nozzle and a focused laser beam. The material is ejected from a nozzle and converges at the surface of the substrate, it is then melted to the layer below by a focused laser. The lasers involved in this process are typical of similar quality to the powder bed process exhibiting Yb:YAG fibre lasers of 200 to 400 W. The powder/wire feed process can be categorized into three main systems: direct energy deposition, laser metal deposition and laser cladding.

Direct energy deposition (which is inherently the same as laser metal deposition) is a method of additive manufacturing where a powder or wire feedstock is applied to a molten field where it is joined to the layer beneath it. This process is repeated many times over to create a complete, three-dimensional component [26]. Because of the nature of this process, it seems to be well suited for an additive repair field, having the ability to print on, effectively, any form of surface. Figure 3 depicts two variations of the direct energy deposition method [27].

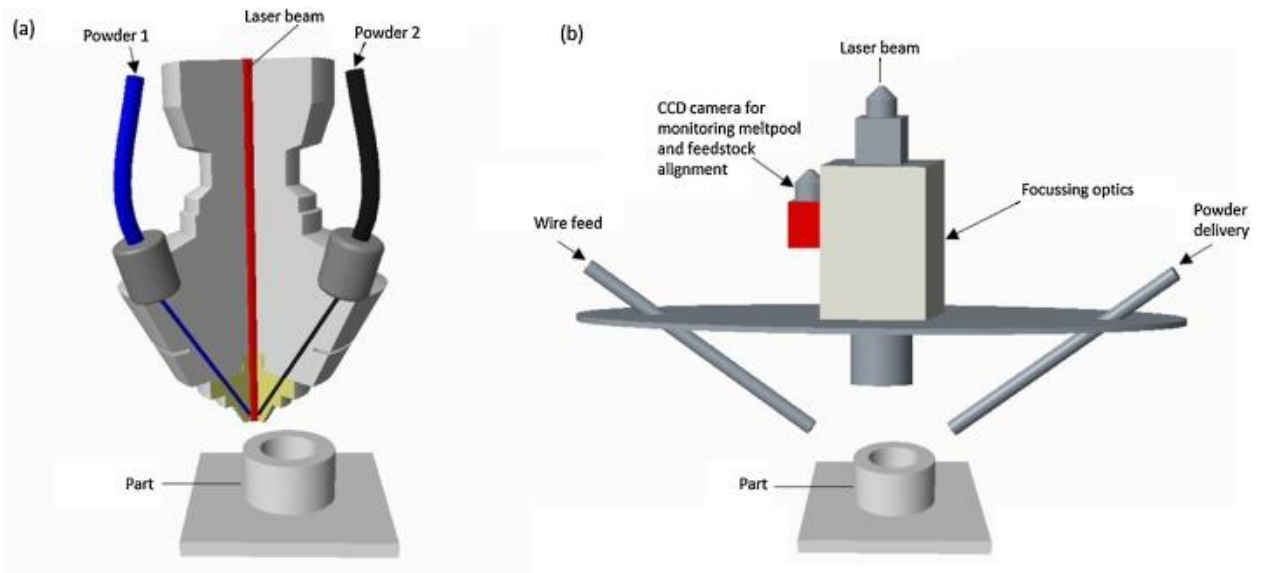


Fig. 1-3 Schematics showing the two principal methods of material delivery in DED for functionally graded material creation: (a) Coaxial multiple powder delivery (b) Wire and powder side fed delivery [24].

Laser cladding is a powder additive process; however, it is used for coating materials. This process metallurgically bonds a thin layer of a material, or alloy, to a substrate. The purpose is to increase the surface properties of the material. Therefore, materials that are low cost can exhibit some properties beyond what they could before. For example, grey cast iron coated with titanium-carbon exhibits better wear resistance. However, using this process can also promote repair of material by melting surface cracks causing them to close [28]. This is another useful method for the repair of components [29]

Electron beam melting (EBM), much like selective laser melting, uses a powder bed system to build a part layer by layer. However, to fuse the layers together an electron beam inside of a vacuum is used. For some materials more susceptible to rapid cooling, electron beam additive manufacturing is more appropriate because it is possible to use the beam to increase powder bed temperatures up to 800-1000 degrees Celsius. This lowers

the thermal gradient and prevents the material from fracture during cooling, when high residual stresses are present. Using EBM, it is also possible to apply a wider range of energy, as the printers can reach powers upwards of 100 watts, making it more promising for printing high melting temperature materials such as titanium, niobium, tantalum, and zirconium [30, 31].

Wire arc melting uses a solid wire of some material that is slowly applied to a region characterized by an electric arc between two points. This process can be described using two types; Gas Arc Additive Manufacturing and Plasma Transferred Arc. Wire arc melting closely resembles welding, except the entire component is made from a weld, rather than bonding two pieces together. This is especially the case for gas arc, as these methods include Tungsten Inert Gas (TIG), which is a common form of welding. Plasma arc, however, increases the temperature of the system to provide more stability. Gas arc melting requires constant monitoring, as there are several dependent parameters that must be closely watched to achieve suitable solidification, plasma arc offers the potential to automate the system, having fewer complex variables that need to be closely observed [32].

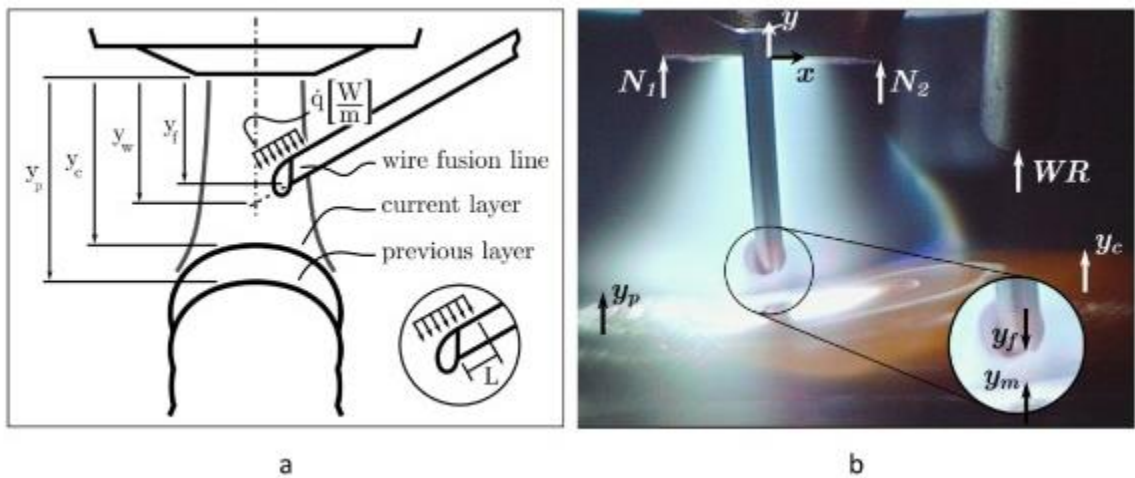


Fig. 1-4 (a) Schematic diagram of plasma deposition showing the position of the wire relative to the heat source and deposit; (b) a typical frame indicating the points of interest: nozzle position (N_1 and N_2), the

wire reference mark (WR), the previous layer (y_p), current layer (y_c), wire fusion line (y_f), and top of the melt pool (y_m) [32]

1.3.1 Powder Production

1.3.1.1 Gas Atomization

Gas atomization is a process involving a melt chamber, induction melting, gas source, nozzle, collection, and fine powder chambers (figure 11). Much like water atomization, gas atomization is performed by exposing the molten pool to a blast of pressurized gas to create small droplets of metal. These metal droplets form the powder and are collected in the collection chamber. Other, finer powders are carried by the gas and collected at the gas exit [33, 34].

By minimizing the distance between the gas exit nozzle and the molten metal stream, energy transfer can be maximized, resulting in the greatest efficiency [33]. In addition, using a modified version of the melting process known as electrode induction-melting, high resolution powder with minimal impurities may be achieved reliably [35, 36]. This form of symmetrical spheroid powder is ideal for the laser powder bed method, as it promotes proper melting during the exposure stage of printing.

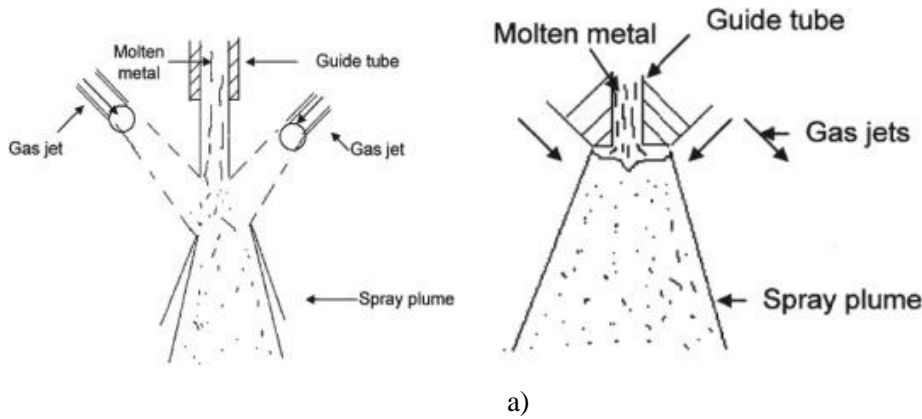


Fig. 1-5 Gas atomization process schematic: a) Free fall gas atomization, b) The process of close-coupled gas atomization [41]

1.3.1.2 Mechanical Milling

Mechanical milling is not a new technology; however, its capabilities are being used to create nanocrystalline powders which can be used in additive manufacturing. Mechanical milling utilizes two pots that rotate, as well as several different balls made of a material that is harder than the material being atomized. The pots rotate and give energy to the steel balls which collide with, and pulverize, larger pieces of the desired material. This process can produce powder comparable in size to gas atomization and water jet atomization, without using large amounts of gas and energy. The produced powder sizes can be less than that of the gas atomization technique, but the morphology is irregular and inconsistent [37].

Fig. 1-6 depicts powder morphology after varying milling times. The mechanically milled powders are significantly more ellipsoid like, which has detrimental effects on the melting properties and solidification because of their uneven melting behaviour. These powders, despite their modified shape, perform with higher levels of ductility and corrosion

resistance, however, coarsening of the grains is often required. [38, 39, 40, 41]. Due to the inconsistencies, these powders are not ideal for LPBF.

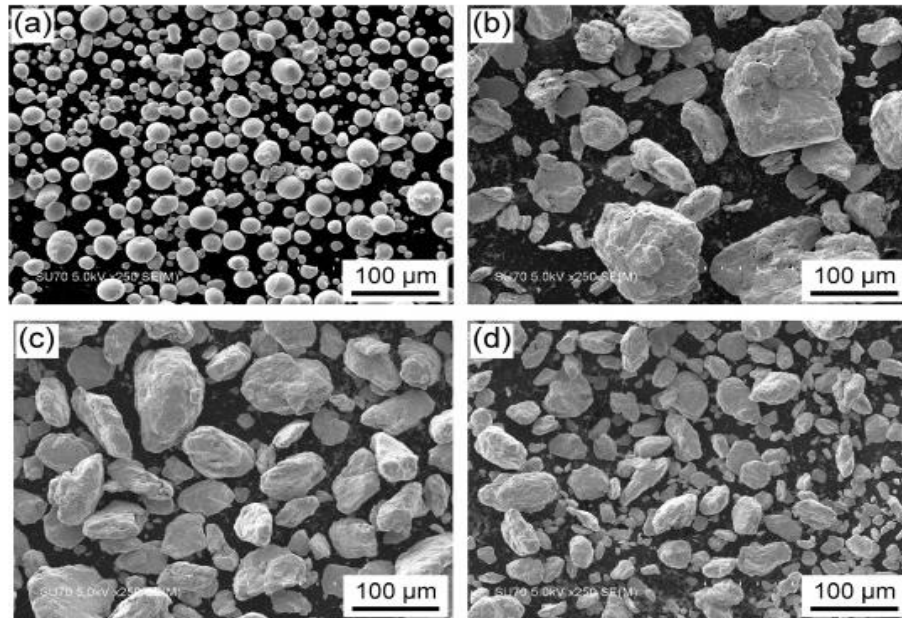


Fig. 1-6 SEM images of the as-received powder and the powders that were mechanically milled for various treatment periods; (a) as-received, (b) milled for 5 h, (c) milled for 10 h, and (d) milled for 20 h [35]

1.3.1.3 Water Atomization

Water atomization is commonly used to produce iron alloy powders; however, it can be used for other low-carbon alloys as well. The process uses molten metal that is poured into a bed and passes through a funnel. Exiting the funnel, the molten metal falls and converges with two jets of water that separate the molten metal into beads, rapidly cooling it and forming a powder. Fig.1-7 shows a schematic of the water atomization process. Powder created using this process has a large fraction of particle size in the 63-150 μm region. This process uses the lowest capital cost and is best used for high volume requirements [42, 43].

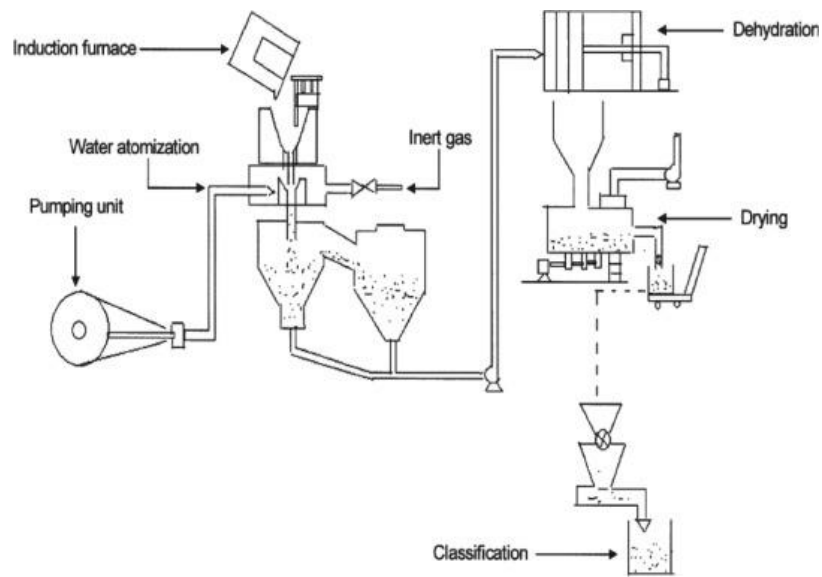


Fig. 1-7 Water atomization process [41]

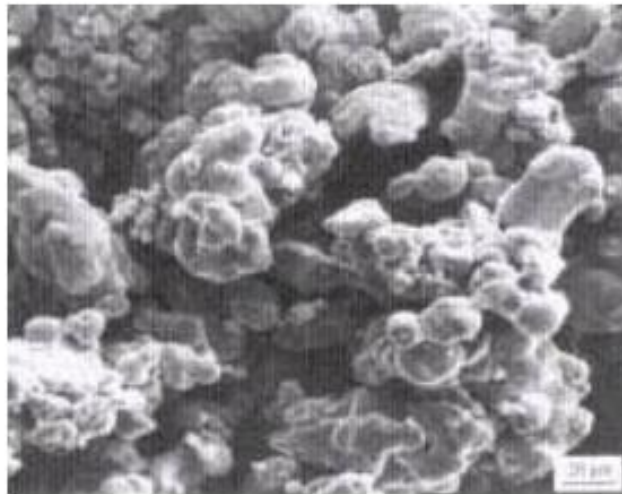


Fig. 1-8 Water atomized powder morphology [39]

Fig. 1-8 shows the typical morphology created by water atomization. The morphology, in this case, is jagged and irregular, similar to the milling process. Morphology during the water atomization process is driven by several factors including, viscosity, jet length, pressure, and angle of incoming jets play a factor. For sphericity, metal surface tension,

temperature gradient, angle of incoming jets and velocity [44]. Irregular geometries are not ideal for powder-based AM as they allow for crevices where powder does not get melted leaving voids, increasing potential crack locations and stress concentrations.

1.3.1.4 Energy density and optimization of process parameters

Additive manufacturing is a complex process involving many variables that influence the solidification, energy absorption, and ultimately the final microstructure of the material being used [45]. Parameters that influence the overall quality of the component range from powder morphology, inert gas environment (Argon or Nitrogen), laser power, scanning speed, scanning strategy, amongst others. Parameters primarily investigated in additive manufacturing are those that have a direct effect on the amount of energy absorbed by the system; these determine the melting and ultimately the solidification behavior of the material [46, 47].

$$E_d = \frac{\rho}{v \cdot d} \quad (1.1)$$

where E_d is the area energy density in J/mm^2 , ρ is the power in watts, v is the laser speed in mm/s , and d is the layer thickness in mm .

Eq. (1.1) can be modified to the energy density over the volume E_v (J/mm^3) as Eq. (1.2):

$$E_v = \frac{\rho}{v \cdot h \cdot t} \quad (1.2)$$

where ρ is total power supplied by the laser, v is the laser speed along the surface of the substrate, h is the hatch distance, and t is the layer thickness. However, the process is not so simple and involves complex heat transfer, and thermal induced flow phenomenon.

To show that the impacts of the laser power and scan speed on the machine influence output quality, several published works were reviewed. This highlighted the importance of studying scan speed and laser power. Of course, this can vary from machine to machine and vendor to vendor.

Fonseca et al. explored the effects of laser power and scanning speed on AISI H13 tool steel. Figure 12 depicts regions of optimal parameter density surrounded by areas of decreased density. Total energy density dictates the porosity in the component; as the overall energy density deviates from the optimal, it can be seen to decrease significantly. The region of optimal density is quite small based on the experiments conducted. Spanning from 88 to 100 J/mm³, with laser powers from 130-150, however, there may be a combination of parameters not explored that may yield a more successful result [48, 49].

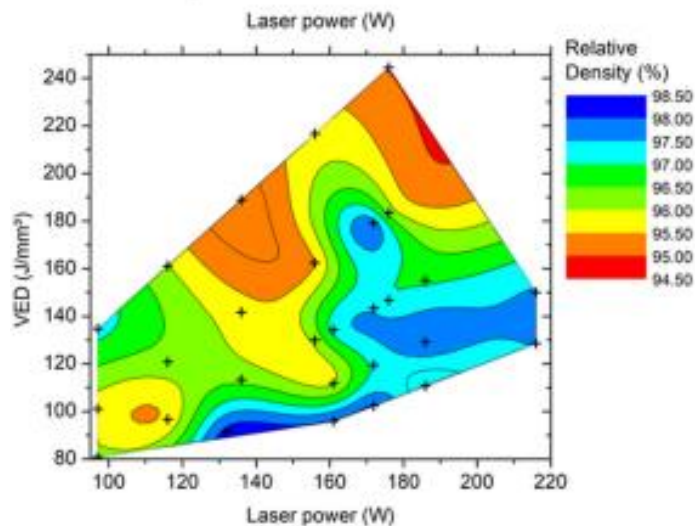


Fig. 1-9 Laser power vs. Volumetric Energy Density in J/mm³ and the resultant density [47]

Sun et al. performed X-ray analysis on the powder and as built samples of powder bed fusion H13 tool steel. Despite similar energy densities, samples exhibited different microstructures. Samples with energy densities of 42.2 J/mm^3 and scanning speeds of 600 mm/s showed additional phases of $\text{Zr}\alpha$ in the 103 orientations, in addition, the higher energy density with the same scan speed presented more $\text{Zr}\alpha$ of the 1 1 0 orientation. The presence of additional $\text{Zr}\alpha$ (110) led to increased slightly increased elongation performance [50]. The differences, despite similar energy densities, can be explained by Gaussian laser behavior in welding which shows that laser power has a greater effect on the melt pool [51, 52, 53].

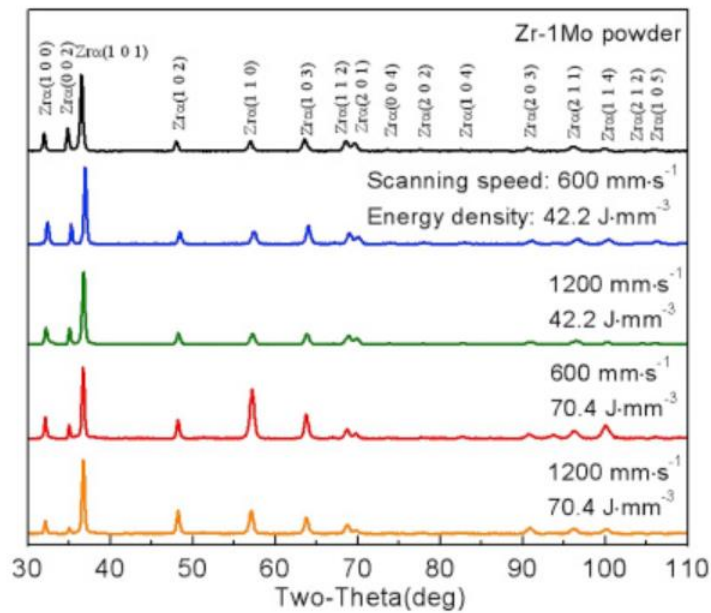


Fig. 1-10 Assessment of laser power and scan speed influence on microstructural features and consolidation of AISI H13 tool steel processed by additive manufacturing [50]

Ahmadi et al. [54] varied exposure time and laser power with a biomaterial to develop the curves seen in figure 14. By varying these parameters greater density can be

achieved and is directly reflected in the yield stress; as density increases, yield stress increases [54, 55].

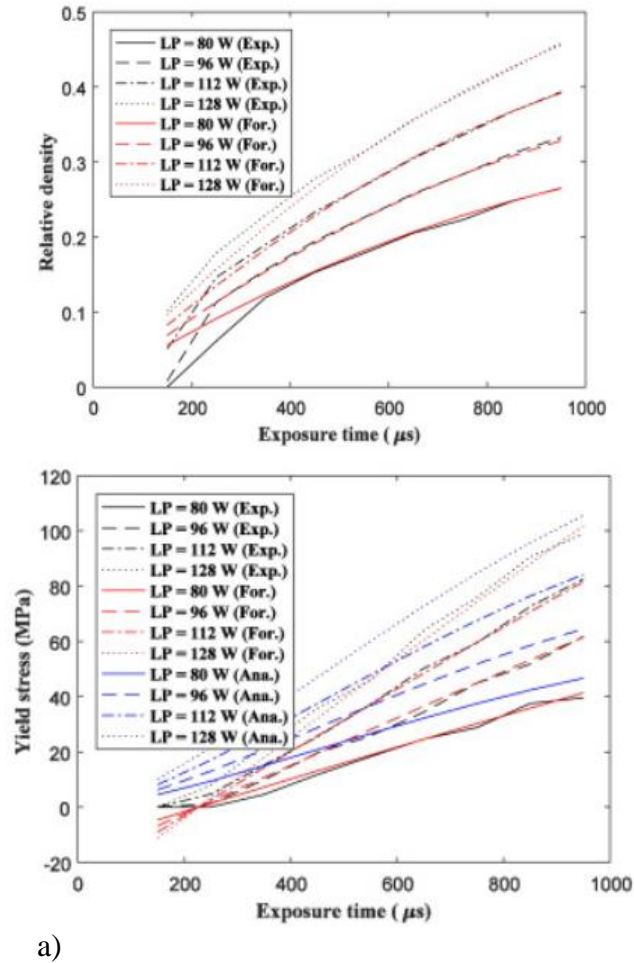


Fig. 1-11 Comparison of geometrical and mechanical properties curves of different processing parameters between the experimental results, empirical formulas, and analytical prediction: a) relative density, b) yield stress [51]

Carlton et al. [56] explored the effects of porosity and heat treatment on the austenitic 316L stainless steel using the SLM process. As-built samples showed up to a 40% increase in engineering stress compared to those of the wrought material. After annealing treatment, the as-built samples maintained a 20% increase in strength over the wrought material and

increased the elongation from 30% to 75%. The increase in elongation is directly related to the grain regrowth during this process. The as-built samples showed cellular and dendritic cell structures that are indicative of rapid heating and cooling cycles; small dendritic spacings correlate to higher strength [57, 56]. After annealing these grains become larger and more homogenous [56, 58].

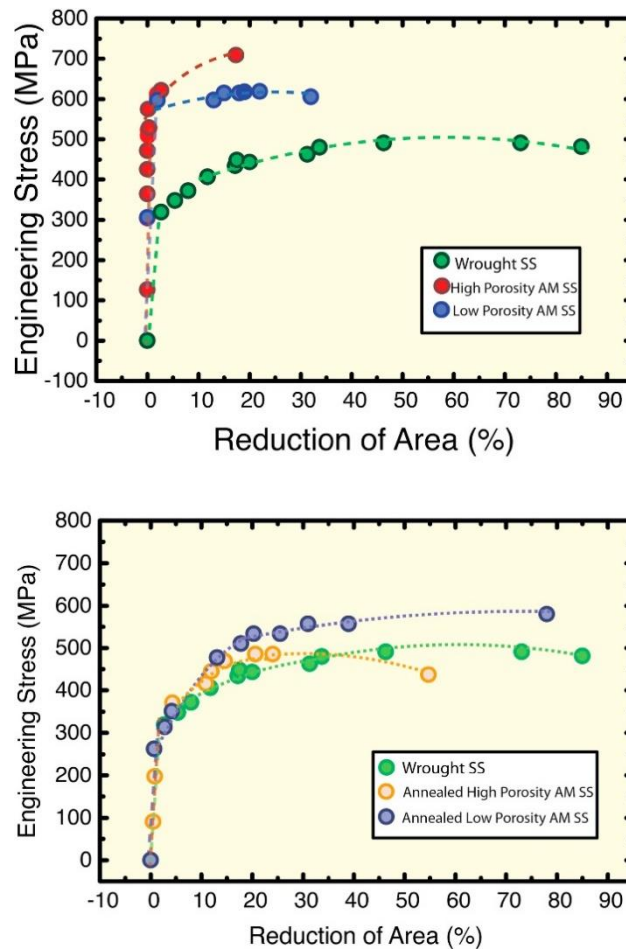


Fig. 1-12 Results from in situ tensile tests. Engineering stress versus reduction of area for the wrought versus as built and the wrought versus annealed samples [53]

1.3.1.5 Process Induced Defects

Process defects can be affected by machine specific differences, including hardware differences, software optimizations, and dead zones. Parameters like power output and laser speed can be affected by lens imperfections, delays, acceleration errors, and other mechanical movements that could inhibit the laser.

Identifying the region of optimal parameters can be quite difficult and demands a large amount of testing. To identify a region of potential interest, the two main defects caused by parameter modification can assist; these are balling and keyholing. Identifying these defects exposes the two extremes of a window in which the optimal parameter set lies.

Melt pool morphology is a critical part of evaluating the quality of AM component and examining it for defects can prove challenging. The shape of the melt pool influences the overall porosity and integrity of the final product [59]. Figure 16 depicts various shapes of melt pools. Comparing the others to image a), the defects are quite pronounced. However, these are single tracks; identifying these defects in a finished component can be difficult, as destructive testing is necessary to draw out the boundaries and locate the fine, dispersed pores that can be created during the SLM processing [60]. It is thus more effective to prevent the formation of such defects by employing appropriate parameter sets.

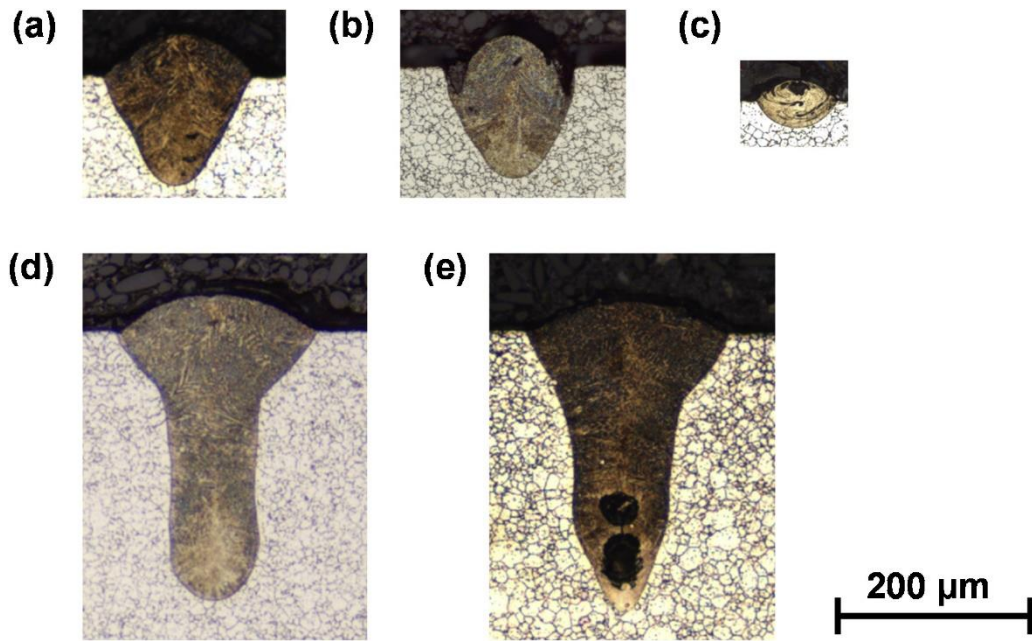


Fig. 1-13 Representative examples of cross-sectional melt pool morphologies. (a) desirable, (b) balling, (c) under-melting, (d) severe keyholing, and (e) keyholing porosity [57]

Balling is a phenomenon that can occur during the SLM process which creates a spherical droplet of molten material (Figure 17). The processing error occurs when melting occurs irregularly, often occurring because the scan speed is too high and creates splashing. Balling adds additional vacancies and uneven cooling resulting in lower density and lack of fusion [61, 62, 63]. Most often this phenomenon occurs because the energy applied to the system is too little and can be fixed by increasing laser power or by slowing the scan speed down, increasing energy density, however it is possible to occur at higher powers as well. [64]. This is another reason to obtain comprehensive knowledge about laser power delivery and the scan speed of the machine of interest.

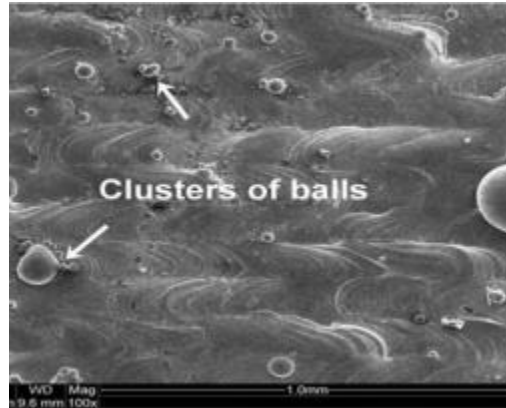


Fig. 1-14 Balling defect under SEM [61]

Similar to balling, lack of fusion (LOF) defects happen because the energy input to the system is too little to sufficiently melt all powder particles, or the overlap of the melt pool leaves a gap of particles that are left un-melted [65, 66, 67]. The pores left from lack of fusion act as crack initiators due to their sharp edges and narrow, dendritic arms [68, 69]. Figure 18 depicts the evolution of pores created by LOF over multiple layers. As layers increase, a compounding effect occurs where molten metal flows around the unfused particles and creates large gaps spanning layers in thickness [65] weakening the product significantly. Lack of fusion can be mitigated by increasing energy densities via laser power and speed manipulation to produce a desirable melt pool with appropriate melting overlap [70]. A similar effect would be observable with gases trapped in the powder during manufacturing. This can be mitigated by pre-drying the powder before use in an inert environment [71] which necessitates a good understanding of the machine capabilities and powder production history.

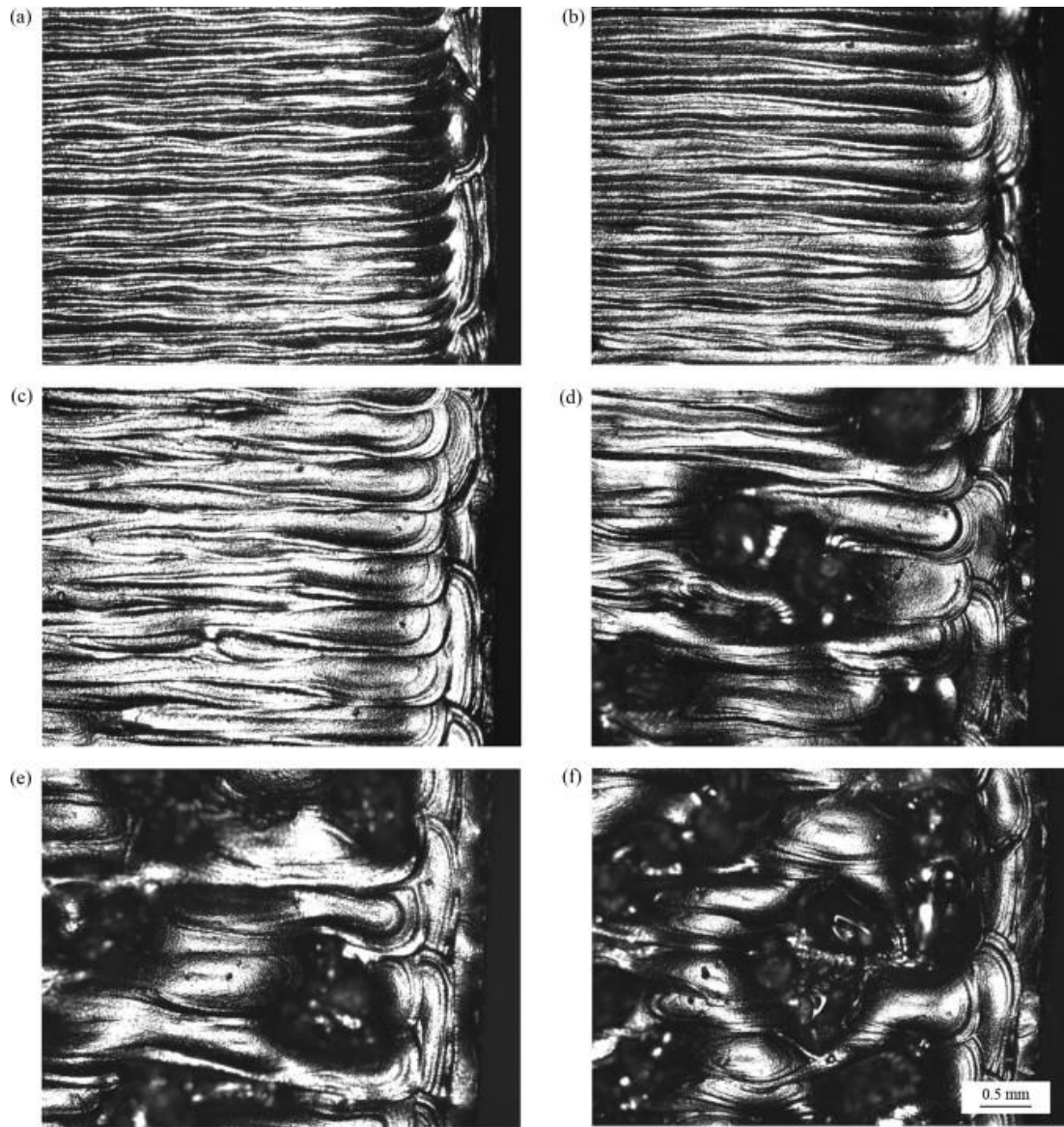


Fig. 1-15 Top surfaces characterization of EBM samples versus line offset (all images are the same magnification). (a) 0.10 mm. (b) 0.14 mm. (c) 0.18 mm. (d) 0.22 mm. (e) 0.26 mm. (f) 0.30 mm. [55]

Keyholing occurs when the energy applied to the system is too high and causes evaporation of the metal, meaning that you have reached or are beyond the upper limit for parameters [21]. Thermal pressures caused by the high energy intensity can create openings for gases to become trapped underneath upon melt pool collapse creating a more porous specimen [72, 73, 74]. Figure 19 depicts the shape of a keyhole melt pool, the primary indications of

this form of melt pool is the depth being significantly larger than the width [75]. By lowering the laser power and/or speed can prevent this type of melt pool from forming. Research on operational capabilities of the machine is the primary method of determining these limitations.

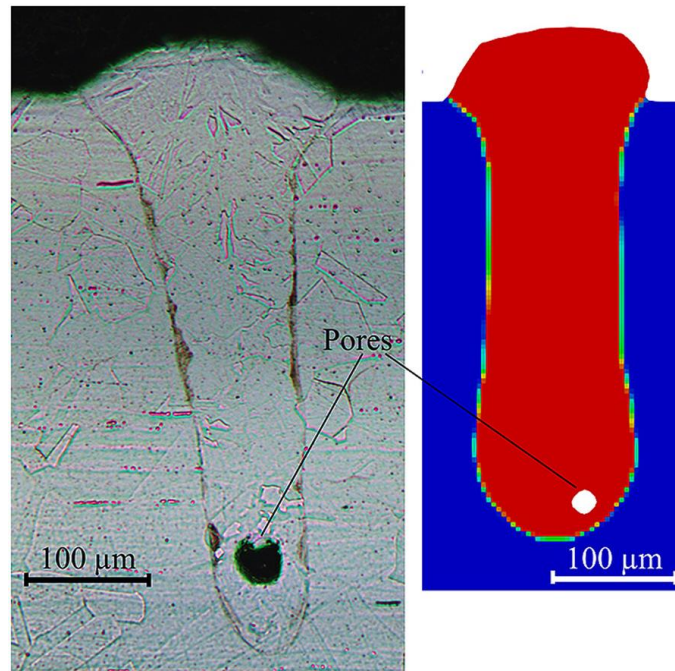


Fig. 1-16 Keyhole melt pool with trapped gas pore [78]

1.3.2 Maraging Steels, 17-4 PH Steels, and CORRAX™

Maraging steels are a family of steels that contain low carbon and use intermetallic precipitates for strengthening, improving strength, and resistance to damage [76]. Laser power and speed are known parameters that influence the behaviour of the material and have been well studied with maraging steels. This makes maraging steel an ideal candidate for use in this study and testing the parameters of the machine.

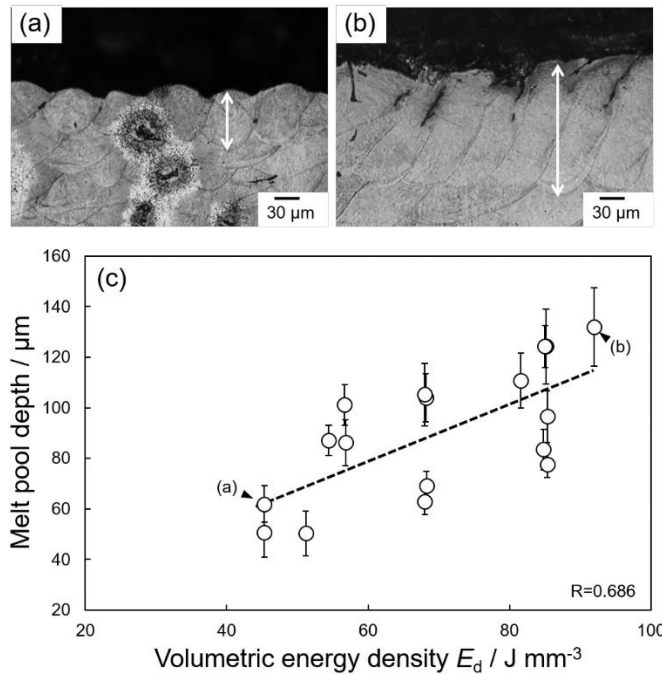


Fig. 1-17 (a, b) Optical microscopy images (a) 170 W and 2500 mm s⁻¹ and (b) 230 W and 1667 mm s⁻¹; (c) change in melt pool depth as a function of volumetric energy density [81].

Figure 20 shows the variation in volumetric energy density vs melt pool depth. Generally, increasing energy density shows a greater melt pool depth, however, between 50-60 J/mm⁻³ and 80-100 J/mm⁻³ there are similar energy density values with differing melt pool depths. This is evidence of the unreliability of energy density as the only factor affecting the resultant melt pool form. However, this parameter sets a baseline for further exploration.

CORRAXTM belongs to the maraging steel family, however, it contains 11% chromium and less nickel, which is different from maraging steels like 13-8 PH, or 17-4 PH. High hardness, strength, and additional corrosion resistance make CORRAXTM of particular interest to industries which include marine, nuclear, and chemical which require long life cycles under highly corrosive conditions. Asgari et al. (2018) noted that CORRAXTM has

not been studied under desirable parameters for general applications, where a limit in terms of hardness, toughness, or strength can be identified. [77]. These types of maraging steels attribute their superior strength to precipitation hardening (PH) mechanisms that occur during deformation.

During additive manufacturing, the rapid heating, and cooling rates (up to 10^6 K/s) generate unique microstructures. Maraging steels primarily are composed of a martensitic structure that is identified by its needle like appearance. Fig. 1-21 shows the martensite present around the melt pool border. The presence of additional austenite (γ) takes up the additional space within the melt pool. The austenite can be attributed to a lowered martensite start temperature which can be related to the lower grains produced from the AM process [78, 79, 80]. Columnar structures (M) are known to form along the grain boundaries, however towards the core of the melt pool a cellular structure (C) is formed [81].

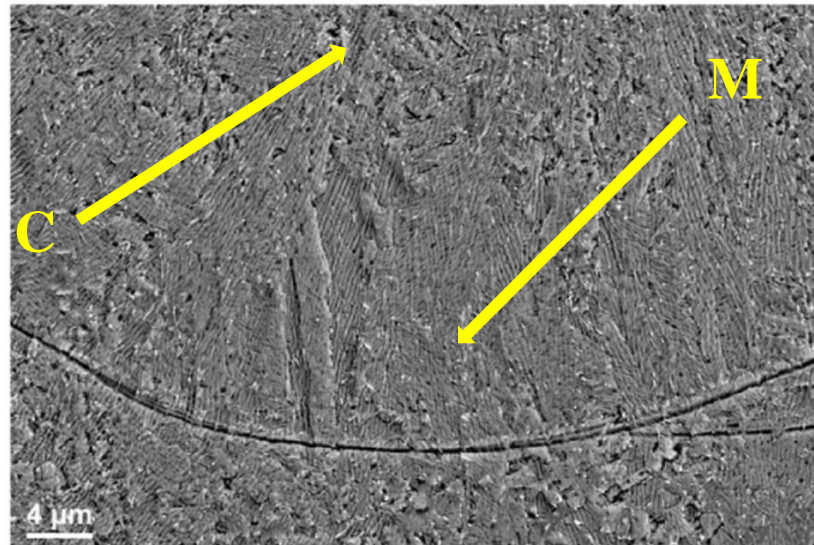


Fig. 1-18 Columnar and cellular structure present in Corrax® [78]

Chapter 2

Experimental Method

2.1 Experimental procedures

2.1.1 Commissioning of a Laser Powder Bed System

Acquisition and commissioning of an advanced manufacturing laser powder bed system required several steps including acquiring equipment, initial training, and development of the equipment. Significant training and understanding of the process ensure the printer operates in a controlled environment for reliability and repeatable purposes. Site acceptance tests (SAT) were conducted to provide confidence with the manufacturer and insurance of safety. Basic and advanced training was conducted over a year to provide the foundation for the development of material parameters. Software training for the proprietary software Magics for metals applications was conducted. Confirmation of competency was conducted using maraging steel as a test material, followed by the production of a component using CL-91RW.

Certification training, provided by GE ConceptLaser, consisting of a five-day workshop explaining general use of the printer, safety precautions, sample preparation, build and post build processing was conducted. Safety when handling this equipment is paramount. Metal powders pose many hazards including health and explosion risks, handling materials requires material behaviour understanding. Materials such as aluminum and titanium pose an explosive risk as the light material stays ambient and reacts to oxygen; when disturbed can cause a “dust effect” which is an explosion or flammable hazard.

Advanced parameter training, focusing on the included advanced software package, and modifying parameters for customization and research exploration purposes was conducted to increase foundational knowledge.

Parameters involved in LPBF are complex and numerous, including many exposure elements such as contour, core, upskin, downskin, upsides, and downsides. These elements are segregated to promote the performance and surface finish of the final part. Upskins and downskins are exterior surfaces on the top and bottom of the part. They represent inclined exterior surfaces that, under the same parameter conditions, would exhibit poor surface finish qualities due to deeper laser penetration and melt pool morphology (Fig. 2-1). By adjusting the parameters on these surfaces, more desirable surface roughness can be acquired. Surface roughness and design are important to promote increased fatigue life in AM components [82].

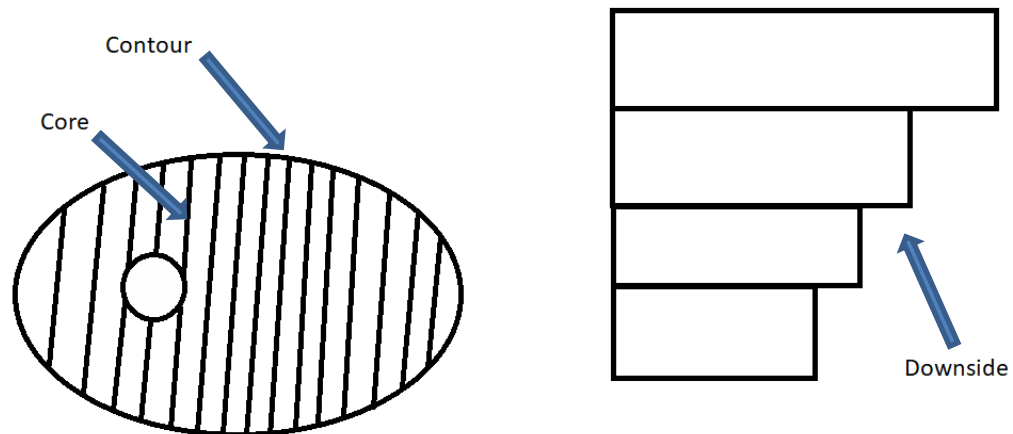


Fig. 2-1 Contour, core, and downside surface elements

The surface pattern exposed is a critical component of the exposure pattern that influences the residual stresses and microstructure of the build. Layers are typically

performed using a continuous exposure pattern that alternates direction; however, additional exposure patterns may decrease or distribute residual stresses in a more desirable manner. Islands exposure pattern divides the cross-section into square components, which reduce the potential for stress-related cracking by distributing the heat input as evenly as possible. This type of exposure pattern can be performed randomly, which evenly distributes the heat input or line by line which would perform similarly to the continuous exposure pattern.

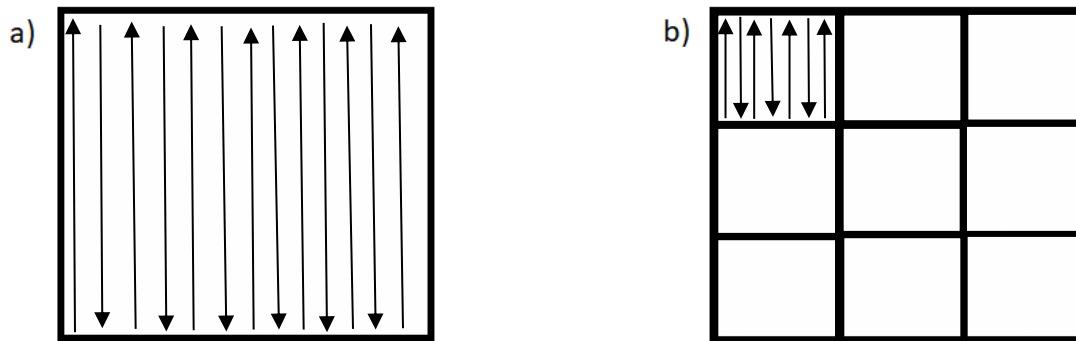


Fig. 2-2 Surface patterns a) continuous b) islands

Within the exposure element, the beam profile is broken down into surface elements. Critical features include the overlapping area, spot size, trace width exposure limit and vector. The overlapping area represents the heat affected zone (HAZ) of the process and is influenced by the trace distance. The trace distance is the distance between two melt pools; this affects the product by increasing the input energy influencing the porosity and integrity. The longitudinal distance is the extension of the melt pool trace width in the direction of the beam affects the geometric accuracy of the build.

Using the gained knowledge of the software, “Parameter Editor,” profiles were created for the required samples and added to the print queue. The parameters were examined and discussed prior to development of the samples. Samples were prepared using the acquired CL91-RW powder. Samples will be built on the provided steel build plates under Argon inert gas. Forty samples of 10x10x10mm will be printed using parameters ranging from 270 to 326 watts and 900-1100 mm/s in increments of 8 watts, and 50 mm/s.

Powder changes are required to ensure minimizing contamination and inconsistencies. Incompatible materials pose various detriments to printed specimens like delamination, galvanic corrosion, and the creation of stress concentrated areas due to insufficient melting. Cleaning of all surfaces in the build path was conducted when switching from maraging steel to 316L, and finally to CL-91RW.

2.1.2 Materials and LPBF process

Gas atomized hot-working steel powder with the brand name CL91-RW, and chemical composition shown in Table 2-1, was used as the feedstock material (Material datasheet, 2018). This powder was previously unused and supplied by GE Concept Laser (Material datasheet, 2018). Samples were printed on a GE Concept Laser M2 cusing machine. This machine is equipped with a 400 W Yb-fiber laser with a spot size of 50 μm . Argon gas (purity 99.999% from Air Liquide) was blown over the build plate during the LPBF process, Table 2-2 shows the laser power, laser scan speed, hatch spacing, and powder layer thickness used to produce forty cubic samples along with associated simplified volume energy densities determined using equation 1:

$$E = \frac{p}{v \cdot t \cdot h} \quad (1)$$

where p is the laser power in watts, laser scan speed v in mm/s, hatch spacing h in mm, powder layer thickness t in mm and E in J/mm^3

Table 2-1 Chemical composition of maraging steel MS1 powder ([83])

Element	Ni	Mo	Al	Cr	C	Mn	Si	Fe
Weight %	9.2	1.4	1.6	12	≤ 0.03	0.3	0.3	Balance

The effect of laser spot size to calculate the energy density is not considered in this equation and was kept constant in this study. A set of forty solid cubes with 10 mm×10 mm×10 mm dimensions were created using the parameters from Table 2-2. Alternating scanning orientation by 67° was employed using a stripe pattern to manufacture the samples.

Table 2-2 LPBF process parameters applied in this research

Sample	p (W)	v (mm/s)
1	270	900
2	270	950
3	270	1000
4	270	1050
5	270	1100
6	278	900
7	278	950
8	278	1000
9	278	1050
10	278	1100
11	286	900
12	286	950
13	286	1000
14	286	1050
15	286	1100
16	294	900
17	294	950
18	294	1000

19	294	1050
20	294	1100
21	302	900
22	302	950
23	302	1000
24	302	1050
25	302	1100
26	310	900
27	310	950
28	310	1000
29	310	1050
30	310	1100
31	318	900
32	318	950
33	318	1000
34	318	1050
35	318	1100
36	326	900
37	326	950
38	326	1000
39	326	1050
40	326	1100

2.1.3 Characterization

The melt pool morphology and density of the CL91-RW were studied using microscopy and the Archimedes Principle. Samples were cut in half using a hand saw and polished for microscopic investigations. Samples were hot mounted first and then polished by a Nano 1000T Grinder-Polisher by employing SiC sandpapers starting from FEPA grade 300 to 4000. The surface finishing was implemented vibratory polisher 0.5 μ m silica suspension. To display the melt pool features for the optical microscope (OM) observations, the samples were etched in Beraha's Tint ($3\text{ cm}^3\text{NH}_4\text{HF}_2 + 25\text{ cm}^3\text{HCl} + 125\text{ cm}^3\text{H}_2\text{O} + \text{Few grains } \text{K}_2\text{SO}_5$) for up to 10 minutes. The LPBF-CL91RW samples were hot mounted, and the image processing was also conducted by employing an optical microscope (OM) to examine the melt pool morphology.

The other half of the samples were tested for theoretical density by employing the Archimedes principle (Fig. 2-1). Utilizing a scale, beaker, and hanging weight apparatus, sample weights were measured and recorded in the air first, then submerged in distilled water, removed, and brushed to remove the air pockets created on the rough surfaces. Samples were resubmerged for measurements.

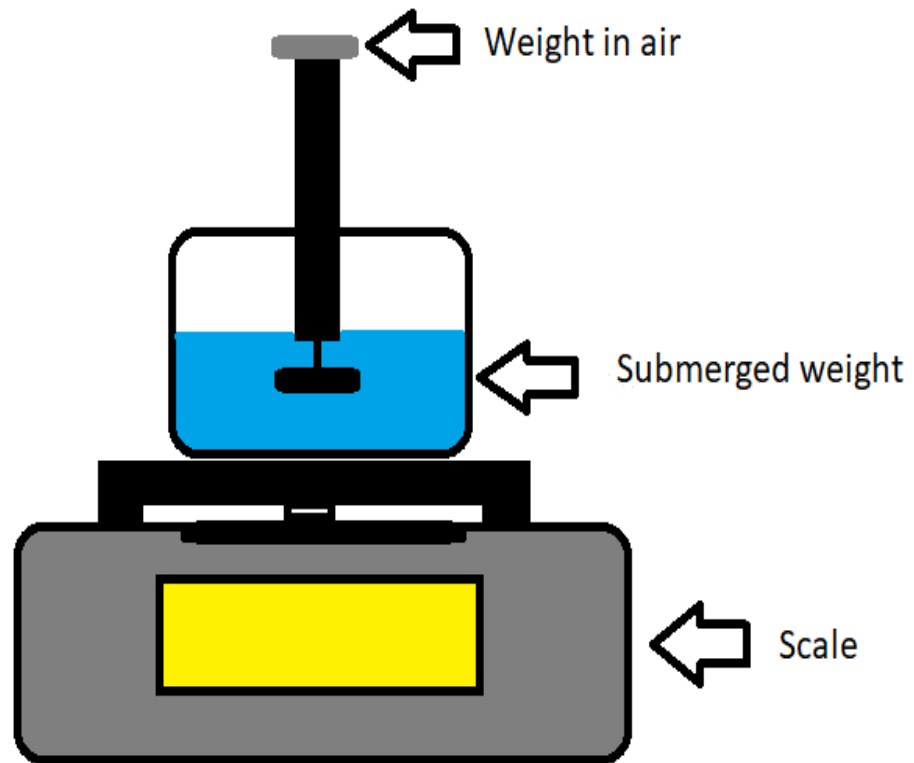


Fig. 2-3 Archimedes Apparatus

Chapter 3

Concept Laser M2 Cusing

The M2 Cusing from General Electric's (GE) Concept Laser is a manufacturing metal 3D printer utilizing laser powder bed fusion. A 400W Yb doped fibre laser is used in conjunction with an automatically adjusted mirroring system to move the laser across the surface of the powder. This machine requires the environment to be inert, therefore it uses gasses such as nitrogen and argon to displace the oxygen preventing defects or oxidation from occurring during the manufacturing of components. During this process complex phenomenon occurs that involves many factors such as Marangoni flow, convection, evaporation, radiation, conduction, surface tension, residual stresses, reflection, and refraction. As heat is applied to the system containing spherical powders, all the listed actions occur simultaneously as the metal powder is heated instantaneously and cooled at rates up to 10^6 K/s. To ensure that the prints run smoothly and there are minimal complications, the set up for the printer is vitally important. Developing a comprehensive knowledge of the machine performance and limitations which enable one to calibrate each print is necessary. The experience and knowledge obtained were accumulated in the frame of a guide. The developed guide also permitted other users to operate and calibrate the machine appropriately. This chapter will focus on the operation of the manufacturing metal selective laser melting machine, the ConceptLaser M2 Cusing.

3.1 Operational knowledge of the machine

3.1.1 Pre-print Processing

Components are first generated within a computer aided design software (CAD) and are converted from a part file into an STL file. STL format meshes the part with a combination of triangles to identify features. The finer the mesh the more details are maintained but the larger the file size, which makes reading the files slower and can affect the cooling behaviour of the print.

STL files are uploaded into a program called Magics made by Materialise. Magics is an editing software that allows for basic CAD construction but focuses on STL editing and build plate preparation for metal 3D printers. When STL files are generated, the transition to other platforms can cause several errors which need to be corrected. Fig 3-1 shows the fixing information for part files within Magics. When correcting errors, it is imperative to begin with the inverted normal and move downward toward edges, and shells to prevent the accidental creation of more errors. Some edges or holes, depending on the desired profile, will need to be fixed using alternate methods and cannot be automatically fixed by the program. Overlapping and intersecting triangles for the purposes of printing are not a cause for concern if Magics allows to slice the part and they do not create any deformities on the surface.

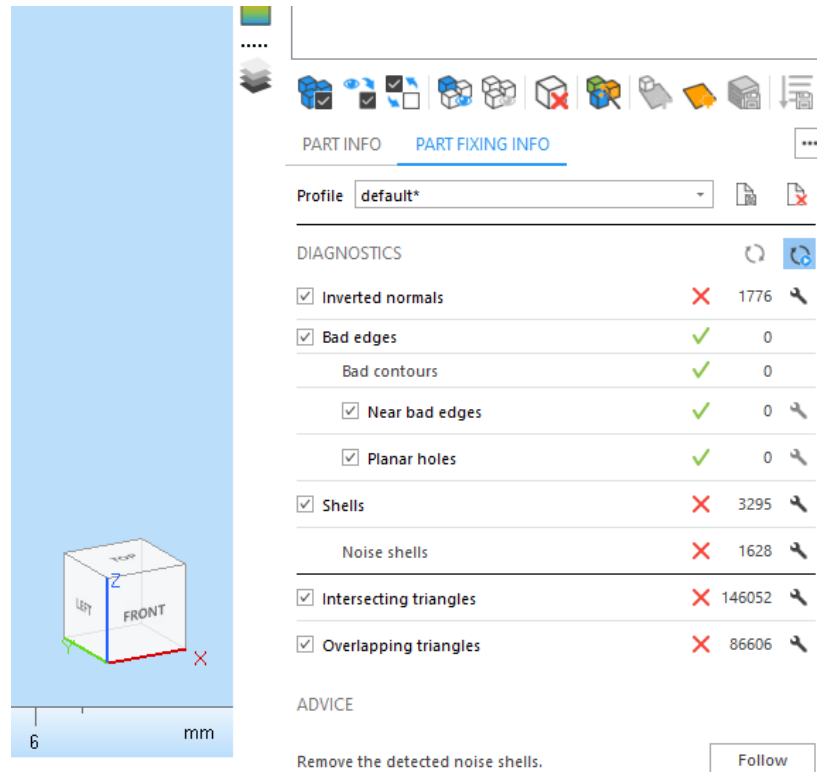


Fig. 3-1 Fixing STL Files

When all errors are corrected, support must be generated for the part. Support structure serves a double purpose. It provides a strong bond to the substrate to prevent warping, and acts as a heat sink to direct excess heat toward the substrate which controls the cooling of the part. In this way, it is vital to ensure that the support is generated appropriately. Support can be automatically generated using pre-set parameters to help guide the process, or by selecting surfaces support can be manually implemented and customized to specific applications. Following the support generation, slicing the files is conducted using the slicing software Magics. Magics is proprietary software developed by Materialise which converts the given STL file format into a ConceptLaser Slicer (CLS) file. Slicing profiles are developed based on material parameter sets and are material specific.

3.1.2 Print Set-up

The printer is split into two sections, the handling chamber, and the processing chamber. Each chamber has a series of steps that are required to ensure the print process is conducted with consistency and accuracy. Missing steps can compromise the integrity of the product which can be dangerous in an industrial environment or cause inaccurate reading which makes illegitimate research.

Setting a print up requires preparing the handling station for printing. The handling station is equipped with a gloved door to allow for safe and secure handling of oxygen-sensitive powder such as titanium and aluminum. Fig 3-2 shows the exterior of the handling station.



Fig. 3-2 Handling station with gloved door

The build plate is a vital component of the build setup. Material compatibility of the build plate and the metal powder used is important as dissimilar materials can lead to the weakening of the support bond and fracture from the build plate causing warpage, artifacts, and possible damage to the printer. In addition, the material of the build plate affects the heat transfer away from the part being built which can change the microstructure. The build plate is held securely using four bolts in a square formation (Fig 3-3) preventing any warpage of the build plate during the build that is caused by expansion from the absorption of heat.



Fig. 3-3 Build plate bolt pattern

Zeroing the build plate is a process of ensuring the build plate is at the calibrated height for the printer. It is conducted by initially using a flat edge to set a “first zero” point, which

is the initial base point of reference. The master recoater blade, which is calibrated to the focal height of the printer, is installed and the gap between the build plate and the base of the recoater blade is measured using feeler gauges.



Fig. 3-4 Master recoater blade second zero check

The build plate is then raised to the focal height; this is called the second zero. The recoater blade to be used is installed and checked using a process known as a light test. A light source (phone, flashlight, etc.) is employed to check the distance between the blade and the build plate (Fig 3-4, Fig. 3.5). Utilizing the knurls located on the blade holder (Fig 3-6), the blade is adjusted until the light is barely visible. Raising the powder chamber at this time is important to determine and attempt to flatten the powder being used; levelling the powder ensures a smooth and even layer application from the recoater during the initial stages of the print.



Fig. 3-5 Recoater blade install

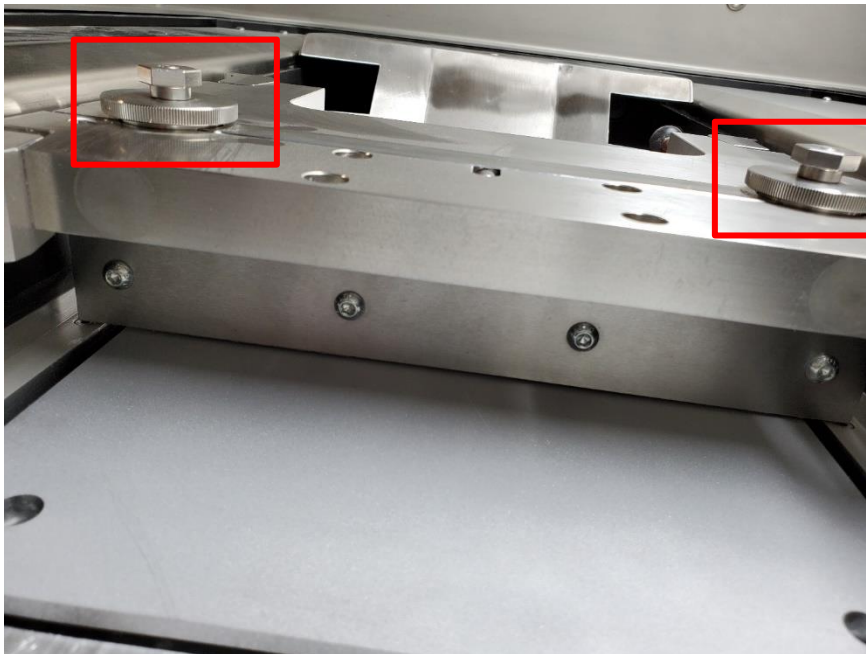


Fig. 3-6 Knurl locations for adjustment

The powder is applied by the recoater from the powder chamber as a “scratch coat,” which is the initial layer of powder applied to the surface that is exposed multiple times to

ensure there is sufficient bonding of the support to the substrate. The substrate should be barely visible through the layer of deposited powder. If the build plate is not level the powder layer will transition to a more opaque and darker grey, where identifying the substrate underneath will not be possible. If this layer is too deep, exposure may not create a sufficient bond with the substrate, increasing the potential for failure.

Moving the technology module into the build station, the environment can begin to be purged using inert gas; the inert gas is typically nitrogen or argon depending on material characteristics and sensitivities. Initial exposure occurs three to five times when the oxygen content in the chamber reaches pre-determined levels. Decreasing the oxygen prevents oxidation and entrapment during the melting and solidification phases.

The desired build job is uploaded to the printer via USB or directly to the printer. The build job, with supports, is imported into the printer where parameters for the environment and build are selected. Environmental parameters control the type of gas and flow rate used for the build. Build parameters control the scan speed, laser power, laser strategy, hatch distance, layer orientation (rotation), and laser on and off times which allows for precision melting throughout the build. The build is started after the exposed surface depicts a shiny coloration.

Completion of the build begins after the build has cooled below 30°C to promote safety when handling the metals. The build plate is raised, and powder is swept into the overflow and stored in a container for post-process sieving. The build is released from the printer by unscrewing the build plate bolts and removal of the part is complete. Using a wet separator, the build is vacuumed to remove any final powder residue. Post processing requirements are conducted including shot peening, annealing, or machining.

Chapter 4

Results and Discussion

4.1 Results

4.1.1 Commissioning

To finalize the commissioning of the metal 3D printer, education with the Magics software and test prints in Maraging steel (CL-50), 316L (CL-20) and CL-91RW were conducted as a test of competency. Starting with a known material such as maraging steel allowed for the exploration of geometries and capabilities of the printer. Switching to 316L enabled experience and familiarity with operating with different materials, observation of behaviour during the printing process, and the exploration of support structures and determination of failure. Finally switching powders to CL-91RW samples were produced to allow for initial microstructural testing.

4.1.1.1 Magics STL development

Imported CAD files to Magics typically contain errors from the meshing process which could show up as artifacts during the printing process or cause disruptions, therefore, it is important to mitigate this concern before the printing begins. Magics is used primarily to fix, slice, and prepare the imported STL files into thin cross-sections that act as guides for the laser during the printing process.

Errors observed during the pre-build process include inverted normal of triangles, stitching errors, and overlapping triangles. Stitching errors cause many surface artifacts and are often simple to fix. Drawing a custom triangle and extending along the hole generated can quickly solve this problem.

4.1.1.2 Part and parameter development

The test plate explored the geometrical limitations of the printer using manufacturer provided parameters. Hole diameters of size 6mm were produced as larger diameters required additional support structure. Round spherical structures, thin walls, thin holes, and structures composed of multiple elements were manufactured to test the combination of complexity. Fig. 2-3 shows the multi-geometrical test plate exhibiting many different simple and complex geometries.

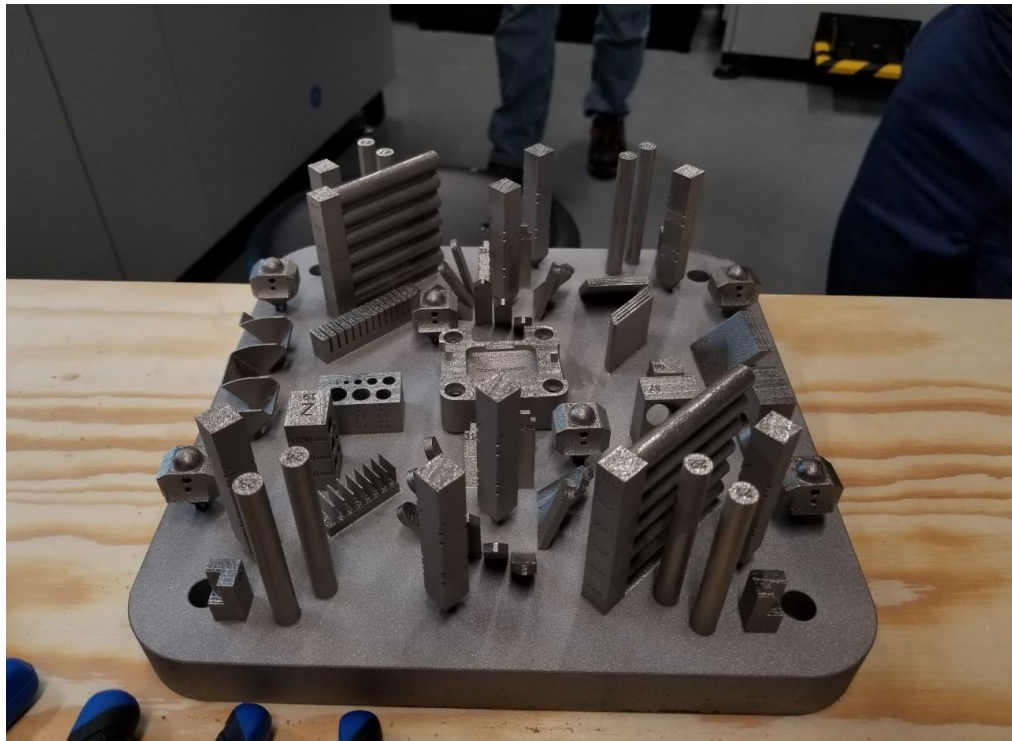


Fig. 4-1 Test plate maraging steel

A part consisting of thin walls and internal structures was printed twice, with and without supports. The experiment found that the unsupported internal structures showed

failure in the form of severe warping and displacement. Compounding errors began to form within subsequent layers likely due to abrasion of the recoater blade from the failed area. In Fig. 4-2 the compounding errors of the internal failure can be visibly noticed. Layer inconsistencies cause areas of the print to get insufficient powder during the layering process. Eventually, the powder getting to this area becomes too thick and insufficient melting occurs. A similar process to printing over fresh powder occurs where there is insufficient heat dissipation and bonding causing warping and further degradation of the recoater.



Fig. 4-2 Maraging steel failed test print piece

A hybrid sample of an injection molding die was produced to test the skill and potential of the process in printing industrial parts. The hybrid sample consisted of maraging steel being printed onto a conventionally produce H-13 tool steel that had been machined into a desirable shape. The top portion of the die included the complex profile of the mold (Fig.

4-3). This process represents a method of repair denoted by additive repair and is especially useful as homogenous material properties can be approached on repaired components promoting cheaper, reliable, and in-house repairs on broken parts [84]. This process tested the accuracy of the machine and the capabilities of the operator.

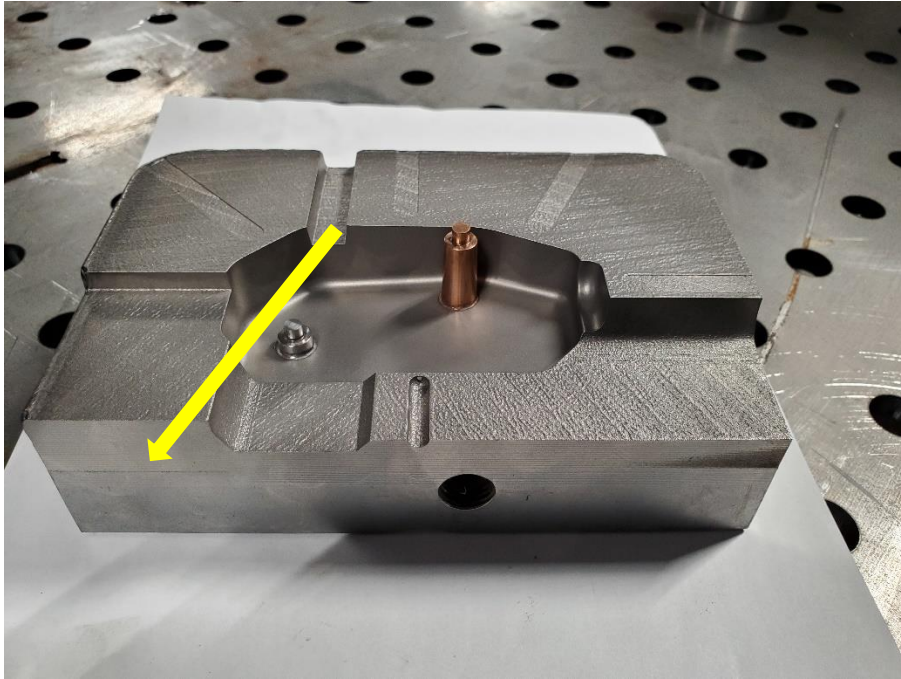


Fig. 4-3 Hybrid injection molding die. Welding seam identified.

Common material, 316L was used as a second steppingstone. 316L parameters are well developed for general purpose. Practice for powder transfer procedures and implementing new parameter processing using manufacturer supplied parameters was utilized. Parts were used to further explore the effects of support structure and limitations of the printer. Fig. 4-4 shows 6 impellers, 3 were printed at 70 degrees and 3 at 45 degrees using altered forms of support structure. Failure occurred in areas unsupported, where exposure surfaces did not have a conductive path to the substrate. The tops of circular holes are susceptible to

this behaviour as well. Warping on the vane entry positions on the under side was observed due to insufficient bonding with “block supports.” Block supports are thin hollow supports that increase convenience as they can be removed by hand but have reduced thermal capabilities which make them susceptible to breaking away from the part.

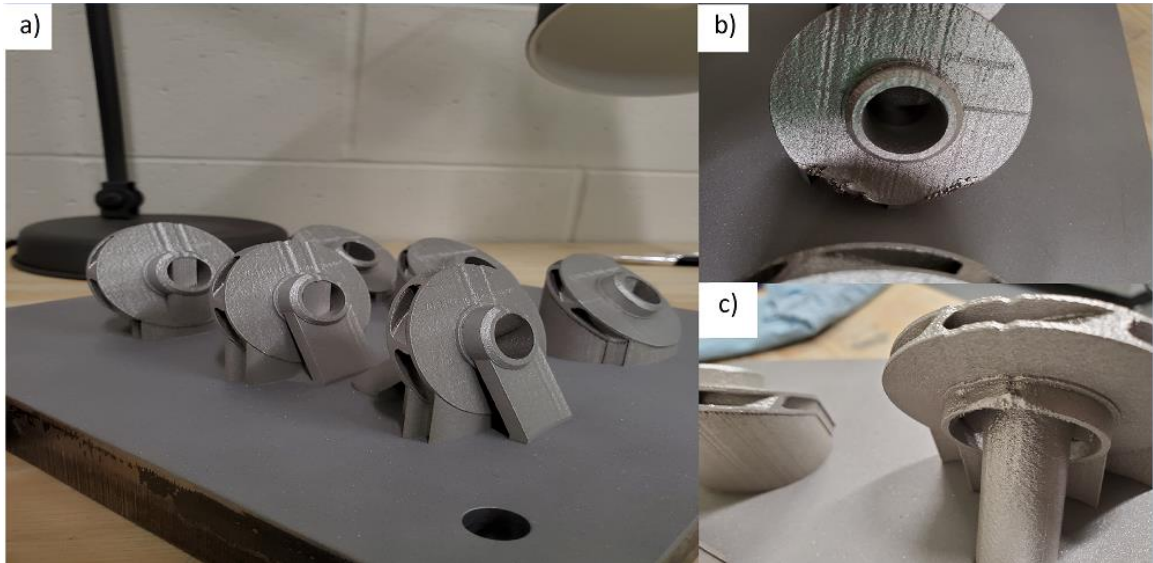


Fig. 4-4 316L print: a) full build, b) Unsupported outer surface failure (45-degree impeller), c) Unsupported hole failure (70-degree impeller)

Completing the build in 316L, and observing the results, a final powder change to CL-91RW was conducted to analyse the effects of laser power and scan speed as they have the most dramatic effect on the energy density equation. CL-91RW had pre-unoptimized parameters from the manufacturer which were selected as the median point for the test. Visually, the samples increased and decreased in roughness as the parameters were adjusted. Fig. 4-5 shows the printed samples. The increase in roughness can be visually identified between samples 6, 16, 26 and 36.

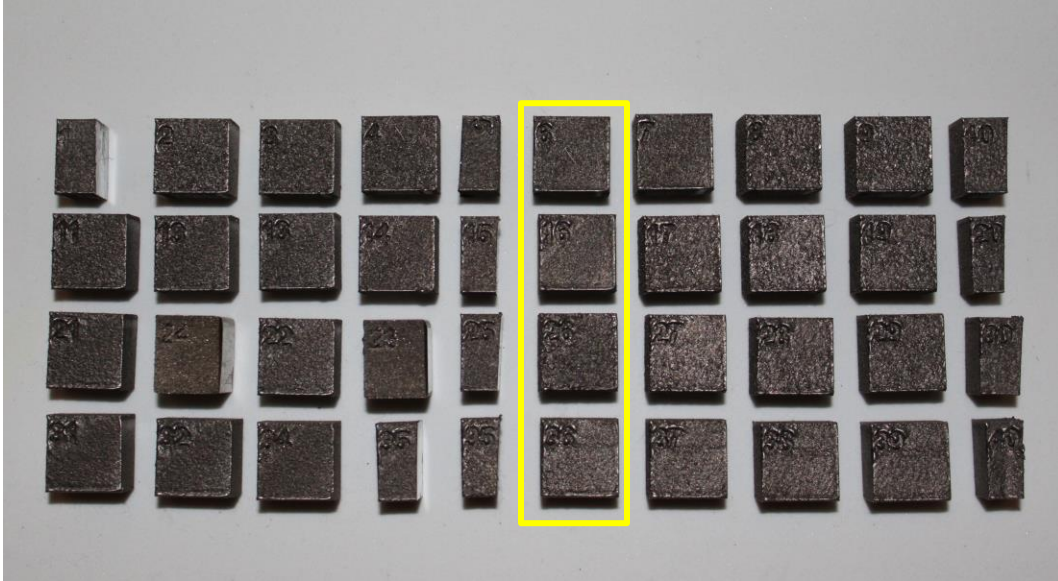


Fig. 4-5 Forty CL-91RW sample printed using varying parameters



Fig. 4-6 Zoomed in samples 6, 16, 26 and 36. Surface roughness can be visually compared

To test the CL-91RW parameters on a component to verify the potential and differences in build from the prior materials, a test part identical to the maraging steel component was created (Fig. 4-6). The part was printed without internal supports. High roughness

was observed, caused by the rough parameter set used ideally for the core. An internal failure occurred; however, the compounding effect was not noticed. Further exploration of the potential for the printing of this material is necessary.



Fig. 4-7 CL-91RW sample print

4.1.2 Density Analysis

Archimedes' principle of density determination uses the difference in the weight of the sample in air and submerged, in addition to the density of the water to determine the density of the sample. Fig. 2-1 illustrates the apparatus used. Equation 2.1 depicts the process of determining density from the recorded measurements. Where ρ_{sample} represents the density of the sample, ρ_{air} is the density of air, $\text{weight}_{\text{air}}$ is the weight of the sample in air, and $\text{weight}_{\text{water}}$ is the weight of the sample in water [85].

$$\frac{\rho_{\text{sample}}}{\rho_{\text{water}}} = \frac{\text{weight}_{\text{air}}}{\text{weight}_{\text{air}} - \text{weight}_{\text{water}}} \quad (2.1)$$

Samples measured were approximately half the size, with some deviations in size that can be noticed in the results, however, size does not influence this experiment. Samples showed densities between 5.42 and 6.32 g/cm³. The weights and densities for all samples can be seen in Table 4-1.

Table 4-1 Sample density and weight in air and water

Sample	Wt. air (g)	Wt. Water (g)	Density (g/cm ³)
1	10.588	8.884	6.205997131
2	6.308	5.166	5.516870746
3	9.154	7.646	6.062849599
4	8.944	7.454	5.995325272
5	9.23	7.707	6.052977032
6	10.1	8.474	6.20394674
7	10.558	8.875	6.265630358
8	9.747	8.119	5.979760552
9	9.848	8.226	6.064072967
10	10.895	9.138	6.193308327
11	8.897	7.429	6.053196375
12	9.153	7.651	6.086403743
13	9.78	8.195	6.162782158
14	11.296	9.504	6.29584325
15	9.852	8.26	6.180855181
16	10.648	8.948	6.255850325
17	9.391	7.851	6.090575736
18	8.873	7.395	5.996022802
19	9.745	8.162	6.148485553
20	7.749	6.418	5.814800696
21	9.461	7.918	6.124044598
22	11.328	9.539	6.324265999
23	9.037	7.551	6.07397082
24	9.532	7.977	6.122388275
25	10.662	8.968	6.286262331
26	9.552	7.99	6.107739595
27	9.133	7.634	6.085258801
28	9.368	7.831	6.087517783
29	9.153	7.644	6.058169928
30	10.174	8.531	6.184739304

31	9.793	8.21	6.178770551
32	8.617	7.187	6.018486404
33	9.283	7.746	6.032283046
34	10.734	9.025	6.273165662
35	11.513	9.394	5.426562087
36	10.005	8.392	6.195123292
37	7.996	6.642	5.898225188
38	9.915	8.307	6.158485205
39	8.975	7.492	6.044502124
40	8.4	6.991	5.954365933

The effect of process parameters on density can be seen in Fig. 2-2 and Fig. 2-3. Samples with 900, 1000, and 1050 mm/s display the close correlation, with 950 and 1100 mm/s showing inconsistent data. Laser power had the greatest effect on density, achieving the maximum density at 302 W and 950 mm/s. Sing *et al.* also showed that laser power had a greater effect on the relative density than the laser scan speed [86].

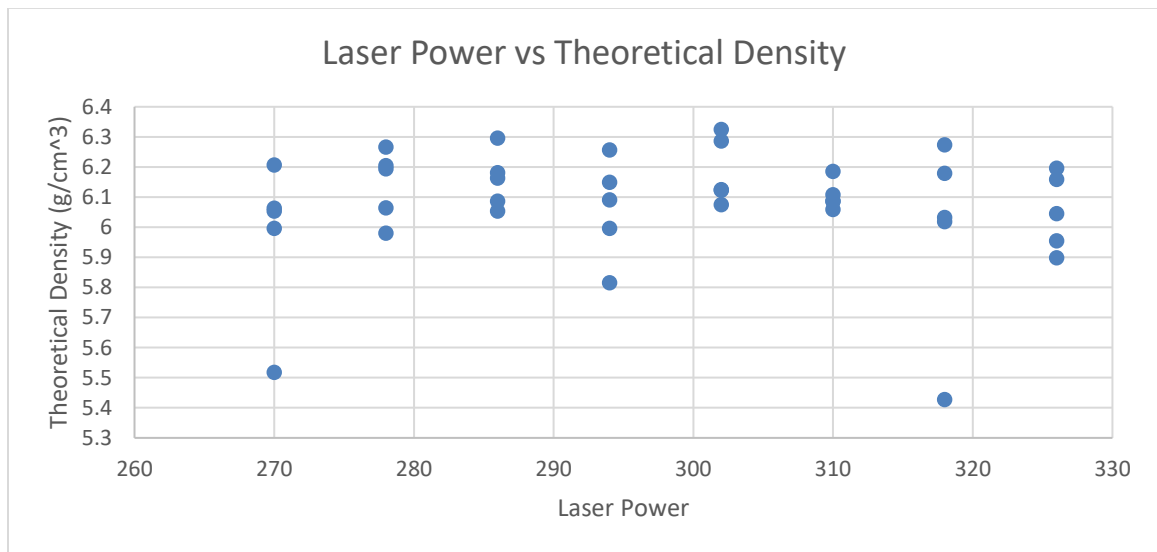


Fig. 4-8 Laser Power vs Theoretical density

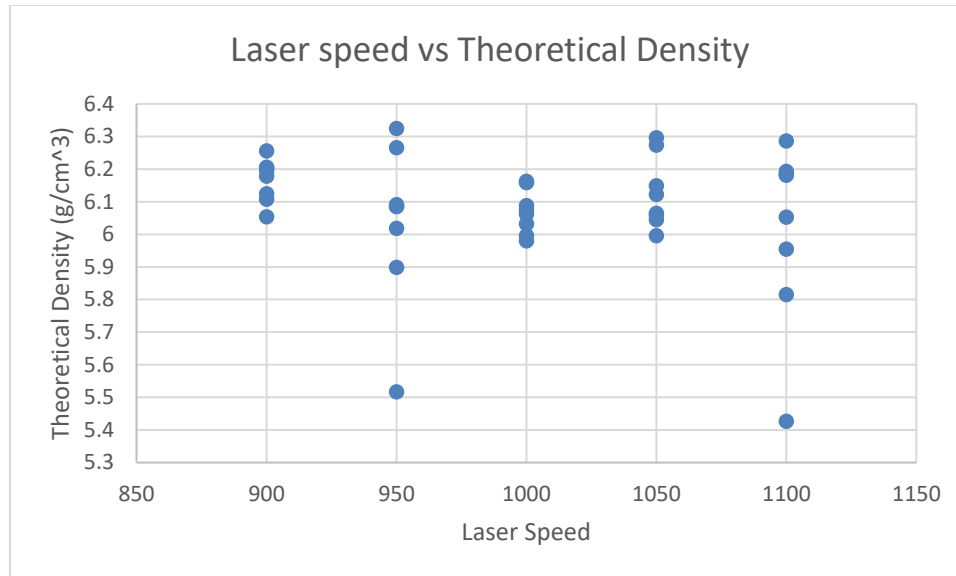


Fig. 4-9 Laser speed vs Theoretical density

4.1.3 Energy Density

Energy density is a measurement that can be used to provide a direct comparison between resulting products such as density, mechanical properties, or microstructure. For every parameter, an optimal combination of parameters can be found. Table 2-3 shows the corresponding sample energy densities which can be used to compare the melt pool morphologies. Energy densities range from 58 to 86 J/mm³.

Table 2-3 Sample and corresponding energy density

Sample	Energy Density (J/mm ³)
1	71.42857143
2	67.66917293
3	64.28571429
4	61.2244898
5	58.44155844
6	73.54497354
7	69.67418546
8	66.19047619
9	63.03854875
10	60.17316017

11	75.66137566
12	71.67919799
13	68.0952381
14	64.85260771
15	61.9047619
16	77.77777778
17	73.68421053
18	70
19	66.66666667
20	63.63636364
21	79.89417989
22	75.68922306
23	71.9047619
24	68.48072562
25	65.36796537
26	82.01058201
27	77.69423559
28	73.80952381
29	70.29478458
30	67.0995671
31	84.12698413
32	79.69924812
33	75.71428571
34	72.10884354
35	68.83116883
36	86.24338624
37	81.70426065
38	77.61904762
39	73.92290249
40	70.56277056

4.2 Discussion

In this thesis, commissioning of the ConceptLaser M2 Cusing was conducted alongside a study on additively manufactured CL-91 RW stainless hot-working steel. The printer was subject to stages of printing and material changes to show competency and consistency in calibration. Test prints using CL50WS and CL-20ES were conducted using supplied parameters followed by samples of CL-91RW with a modified basic parameter. Several modified geometries and a prototype component were used to test the printer. CL91-RW

was investigated by studying elementary microscopic properties including density and melt pool morphology. Samples were cut in half, half was used for the melt pool analysis, the remaining half was used for identifying the theoretical density.

The M2 allows for the customization of many different parameters that affect the processing of the material. Modifying laser power, speed, hatch distance, hatch pattern, gas flow, type of gas, bed temperature, and more can be adjusted to study material behaviour. Training involving parameter effects on printing behaviour and modifying parameters was conducted to ensure competency prior to conducting experiments.

The effects of process parameters on theoretical density were investigated using the Archimedes principle. By differentiating the weights of the sample in air and water, an estimate of the density of each sample was determined and compared to the other samples. A maximum density of 6.324 g/cm^3 was found. Several samples showed densities within 3% of the greatest, spanning across all scan speeds and laser powers. This means that there is an optimal combination of parameters for each speed and power. In this study, the optimal density was achieved with a laser power of 302W and 950 mm/s which resulted in an energy density of 75.689 J/mm^3 .

The process parameters selected were within 10% of the median, as a result, the data collected was difficult to analyze. Using pixels to measure melt pool widths, a trend of increasing melt pool width with increasing power was observed and confirmed in the literature. Examining the low speed and high laser power case in Fig. 2-4, most of the porosity present is centred or below centre of the melt pools which could be a result of the keyhole mode of melting. Recent studies suggest that keyhole modes reduce sensitivities to cracks, however, cause fluctuating hardness values under the keyhole area [87].

Melt pool differences varying laser power observed at 500x zoom are discussed. Fig. 4-9 (a),(b) and (d) all exhibit similar melt pools with narrowing width, (c) shows a wider melt pool. Adjamsky et al. [88] show the evolution of the melt pool with respect to increasing scan speed at constant power. As the melt pool widens, the transition from the keyhole profile to the more desired convective can be discerned [88].

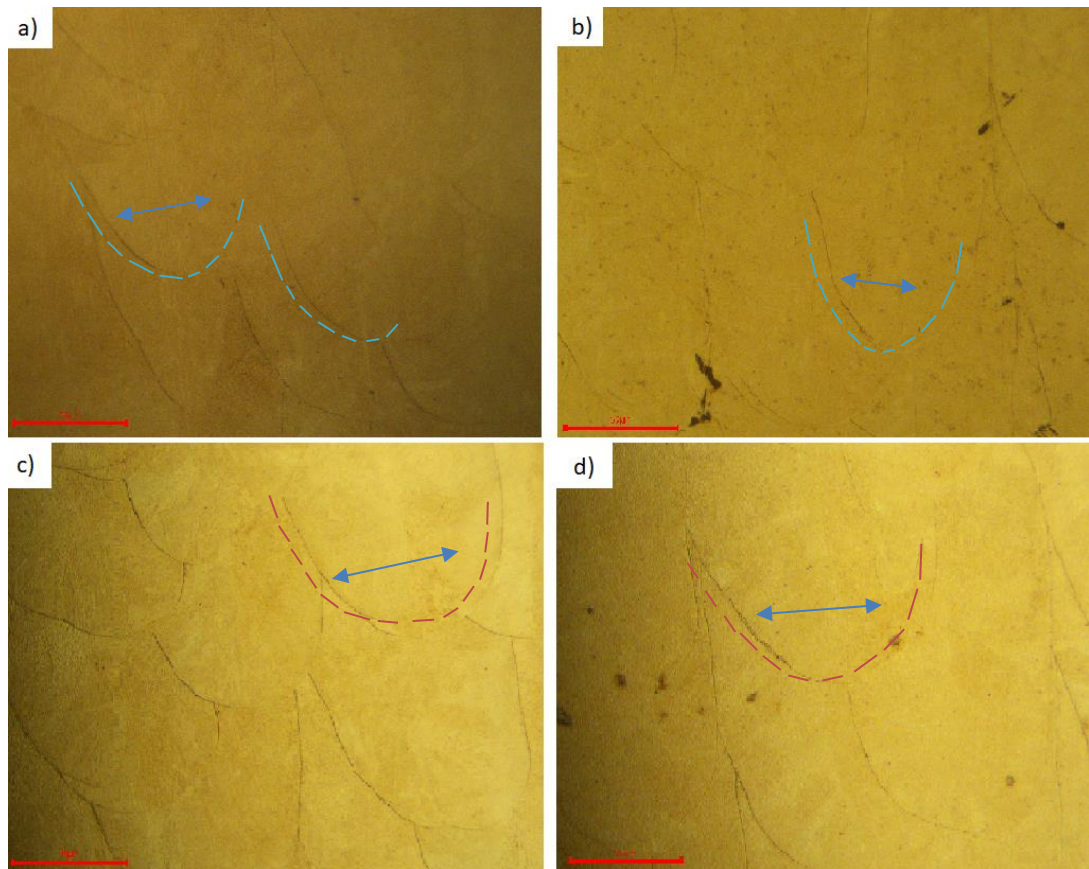


Fig. 4-10 OM images of melt pools with Laser speed of 900mm/s and laser powers as follows: a) 270W, b) 286W, c) 302W, d) 318W. The scale is set to 50 microns.

Examining the melt pools formed by modification of laser power with consistent scan speed of 950mm/s, Fig. 4-10 shows narrower melt pools present in the lower power

settings. Recent studies confirm the correlation of melt pool width to increased energy density but changing parameters [89, 90], table 4-2 shows similar relationships with increasing power. Each measurement was taken at 30 pixels normal to the lower apex on the curve.

Table 4-2 Melt pool width for 950 mm/s scan speed

Sample	Melt pool width (μm)
a	53
b	53.5
c	55.6
d	61.7

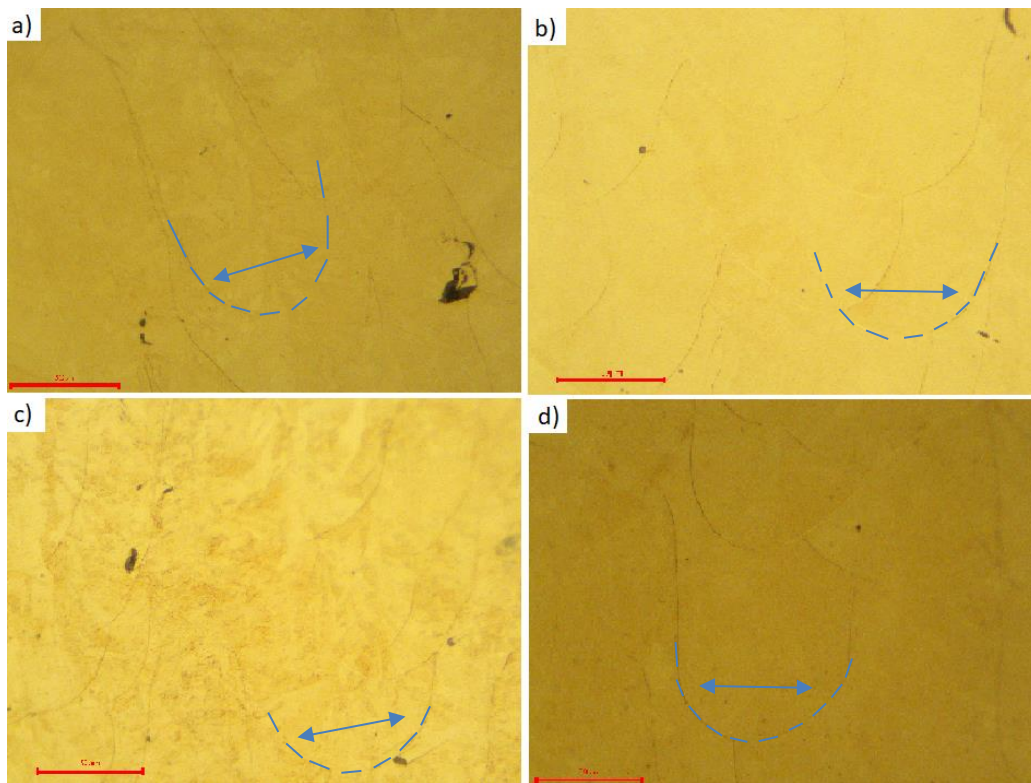


Fig. 4-11 OM images of melt pools with Laser speed of 950mm/s and laser powers as follows: a) 270W, b) 278W, c) 294W, d) 318W. The scale is set to 50 microns.

Fig. 4-11 compares the 1000mm/s samples. Similarly, an increase in melt pool width can be seen spanning from 55 μ m to 70 μ m as power is increased from 270 to 318 W. At the higher energy density slight asymmetry begins to form in the melt pools. Previous studies have shown that irregularities in the melt pools at higher energy inputs are indicators of nearing the transition to keyhole mode [91].

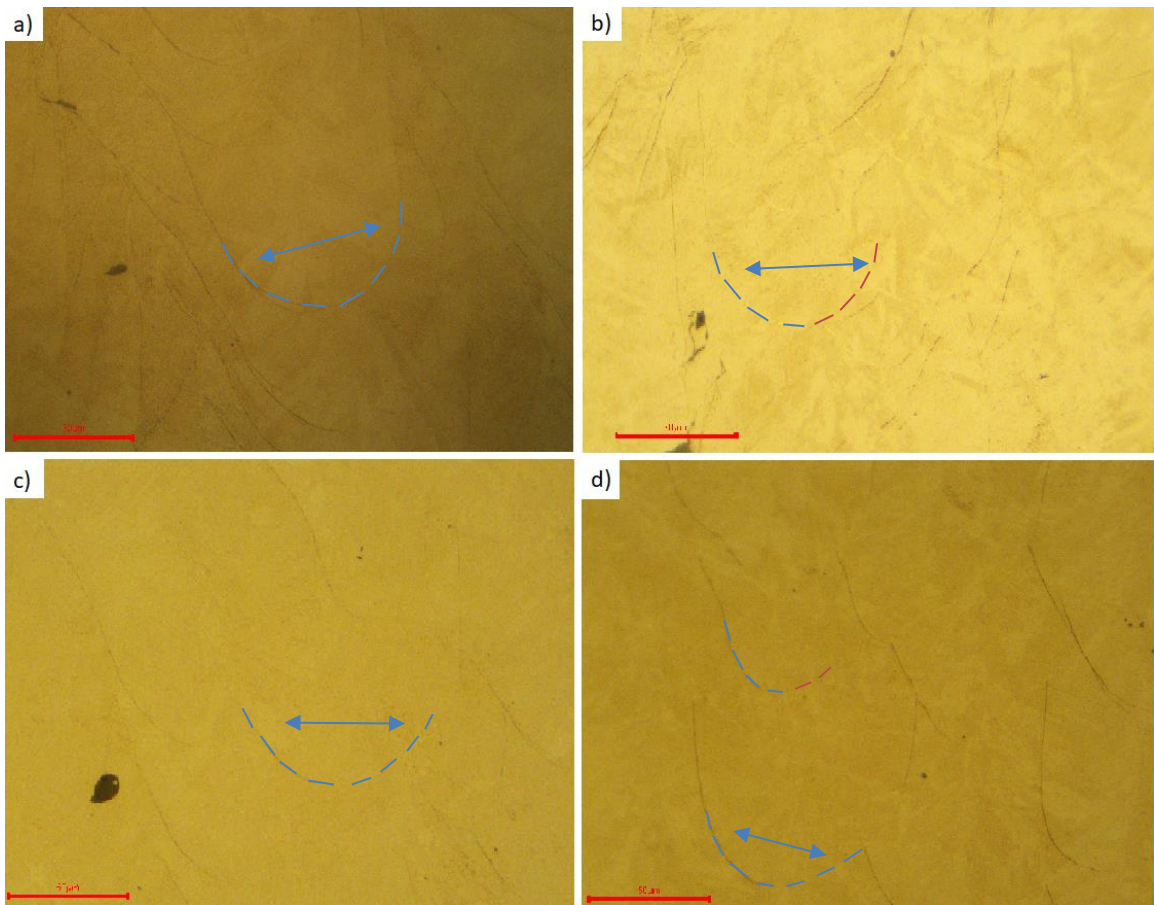


Fig. 4-12 OM images of melt pools with Laser speed of 1000 mm/s and laser powers as follows: a) 270W, b) 278W, c) 302W, d) 326W. The scale is set to 50 microns.

A transition from a rounded needle-like formation to a symmetrical rounded melt pool can be observed in the previous figures and is evidence of the transition between keyhole mode and the desired conduction mode [92]. Modifying the laser speed has a lesser effect

then when the power is modified, in this way, it allows for finer tuning of parameter sets. At lower speeds and higher laser powers, metal vaporization happens creating recoil pressures that trap gas within the melt pools increasing porosity [87]. Controlling this process and preventing vaporization changes the deep melt pools to conduction melt pools that are driven by Marangoni force which appear as shallower, wider, and more rounded [93].

Repeatability in AM has not yet been studied extensively and leaves potential for evaluation [94]. Yakout *et al.* explored the effects of energy density on the relative density of invar and 316L. The study noted that the variation between density was within 2% for varying energy densities [95]. Wang *et al.* [96] showed the variation at of samples within the region of interest showed very little variation in relative density using novel maraging steel. The low level of uncertainty can be attributed to the high level of control over the environment.

Manufacturer specifications for similar materials used currently in industrial applications provide insight into the acceptable regions of uncertainty. CL50WS, a similar maraging steel offered by GE ConceptLaser, has uncertainties for all parameters that reach a maximum of 4% using 45° geometries which are more difficult to fabricate [97]. Experiments performed using the same batch of powder should produce the same characteristics; however, if there is variation in the machine calibration then human error can cause disruptions that modify the result. Other influencing factors such as powder packing factor can influence the propagation of thermal energy through the system [98]. Limiting the potential for variation from human and further errors is important to ensure continuity. Printers, and operator training attempts to remove the potential for packing

factor errors by following appropriate re-coat procedures. Training and comprehension of calibration steps minimizes the variation and ensure reliable and repeatable prints.

Chapter 5

Future works and final remarks

5.1 Recommendation for future work

5.1.1 Exploration of Mechanical Properties and Microstructure

The current work examines the potential for production and application of CL91RW through AM means. To further isolate the optimal region, expansion of the explored window, followed by mechanical testing including uniaxial tensile tests and microhardness can be conducted.

Mechanical testing and failure analysis can determine the differences in ductility and strength for each parameter set identifying a feasible region for commercial application. These tests can also determine if and what phase transformations occur when this material transitions from the elastic to plastic region. Examining the modes of failure, defects, and strengthening mechanisms can determine how viable the parameter set is to commercial application.

The texture is an important microstructural component that can help describe the phenomenon that occurs mechanically and during other processes. By using electron backscatter diffraction (EBSD) and x-ray diffraction, the texture of the material in as printed and post-testing can be determined allowing for a greater understanding and predictability of the material when under loading. Identifying a correct heat treatment can

potentially allow for a tailored microstructure to be more beneficial for a specific application. By varying parameters and testing their strength and texture, this can potentially be applied to the as-built samples increasing their performance under certain loading conditions [99, 100].

Surface finish is an integral component of several parts for many reasons. In terms of mechanical properties, the surface finish has been directly linked to fatigue performance in additive components [101]. Surface finish can be modified by using hot isostatic pressing (HIP) which through heat and pressure close pores on the outer surface and prevent crack initiation. In addition, laser remelting is a process that exposes the surface to lower power, remelting the surface to provide attempt better surface quality. Modifying the flow of the argon/nitrogen can also influence the surface quality [102, 103].

Corrosion for this material is important as it contains elements such as nickel, chromium, molybdenum, and manganese that are associated with performance in corrosive environments. Corrosion testing in combination with texture tailoring could allow for increased corrosion fatigue life.

5.1.2 Modelling and simulations

A crystal plasticity model can be developed to simulate the evolution through phase transformation during loading. Testing samples to develop a physical model would provide a benchmark for the predictive simulation to identify residual stresses and strain localization on the grain scale [104].

Identifying a thermal simulation for this material would be beneficial for the printing of commercial components. Successful prints rely on support structure acting as both a heat sink and adhering the part to the substrate to prevent warping and shifting during the print.

Using thermal analysis and simulation, print reliability and repeatability can be predicted before using the material, increasing efficiency, and reducing risk.

5.2 Conclusions

The project conducted in this thesis investigated the commissioning of a single laser ConceptLaser M2 and the effects of prominent process parameters on the materials morphology and density. A commissioning process involving multi-material and part processing was performed using maraging steel, 316L, and CL-91RW. Initial microstructural testing was conducted to examine the effects of laser power and speed on the relative density of CL-91RW.

Commissioning of the ConceptLaser M2 was conducted using a series of tests consisting of test geometries, sample parts, and support structure requirements for the printed parts. The ConceptLaser M2 showed excellent geometrical accuracy with the printed test plate and hybrid component. The sample part printed in CL-91RW showed less sensitivity to overhang components than the maraging steel, which was evident due to the level of failure seen on the final product. Parts printed in 316L showed the importance of quality support in key areas including overhangs and on low angled surfaces.

Samples produced with CL91-RW using laser powers and speeds respectively from 270-328W and 950-1100mm/s showed a theoretical density within 20% of the greatest density. Melt pool morphologies showed an increase in asymmetry which can also be seen in literature and is indicative of a transition of melt pool mode. Parameters selected were too close together and resulted in similar characteristics across all melt pools with slight changes between the lower and upper power settings.

References

- [1] Government of Canada, "Canadian manufacturing sector gateway," 12 October 2021. [Online]. Available: <https://www.ic.gc.ca/eic/site/mfg-fab.nsf/eng/home>. [Accessed October 2021].
- [2] Next Generation Manufacturing Canada, "NGen whitepaper: Canada's additive manufacturing landscape," 9 December 2020. [Online]. Available: <https://www.ngen.ca/blog/ngen-whitepaper-canadas-additive-manufacturing-landscape>. [Accessed October 2021].
- [3] W. E. Frazier, "Metal Additive Manufacturing: A Review," *Journal of Materials Engineering and Performance*, vol. 23, no. 6, pp. 1917-1928, 2014.
- [4] T. Peng, K. Kellens, R. Tang, C. Chen and G. Chen, "Sustainability of additive manufacturing: An overview on its energy demand and environmental impact," *Additive Manufacturing*, vol. 21, pp. 694-704, 2018.
- [5] J. P. Kruth, M. C. Leu and T. Nakagawa, "Progress in additive manufacturing and rapid prototyping," *Cirp Annals*, vol. 47(2), pp. 525-540, 1998.
- [6] M. Huang, Z. Zhang and P. Chen, "Effect of selective laser melting process parameters on microstructure and mechanical properties of 316L stainless steel helical micro-diameter spring," *The International Journal of Advanced Manufacturing Technology*, vol. 104, pp. 2117-2131, 2019.
- [7] M. Vilanova, R. Escribano-Garcia, T. Guraya and M. S. Sebastian, "Optimizing Laser Powder Bed Fusion Parameters for IN-738LC by Respnse Surface Method," *Materials*, vol. 13, 2020.
- [8] D. S. Shin, C. H. Lee, U. Kuhn, S. C. Lee, S. J. Park, H. Schwab, S. Scudino and K. Kosiba, "Optimizing laser powder bed fusion of Ti-5Al-4V-5Mo-3Cr by artificial intelligence," *Journals of Alloys and Compounds*, vol. 862, 2021.
- [9] A. Kover, "Transformation In 3D: How A Walnut-Sized Part Changed The Way GE Aviation Builds Jet Engines," 19 11 2018. [Online]. Available: <https://www.ge.com/news/reports/transformation-3d-walnut-sized-part-changed-way-ge-aviation-builds-jet-engines>. [Accessed 26 10 2020].

- [10] H. Gong, H. K. Rafi, T. Starr and B. Stucker, "The effects of Processing Parameters on Defect Regularity in Ti-6Al-4V Parts Fabricated By Selective Laser Melting and Electron Beam Melting," *24th Annual International Solid Freeform Fabrication Symposium*, 2013.
- [11] D. Sassaman, P. Hall, S. Fish and J. Beaman, "Two-dimensional Characterization of window Contamination in Selective Laser Sintering," *Solid Freeform Fabrication: Proceedings of the 29th Annual International Solid Freeform Symposium - an Additive Manufacturing Conference*, 2018.
- [12] T. M. Technology, "Types of 3-D printers or 3-D printing technologies overview," [Online]. Available: <http://en.topmaxtech.net/reviews/2015/12/27/types-of-3d-printers-or-3d-printing-technologies-overview/279.html>. [Accessed 21 January 2019].
- [13] A. Fagali de Souza, K. S. Al-Rubaie, S. Marques, B. Zluhan and E. Costa Santos, "Effect of laser speed, layer thickness, and part position on the mechanical properties of maraging 300 parts manufactured by selective laser melting," *Materials Science and Engineering: A*, vol. 767, 2019.
- [14] P. Leo, M. Cabibbo, A. Del Prete, S. Giganto, S. Matinez-Pellitero and J. Barreiro, "Laser Defocusing Effect on the Microstructure and Defects of 17-4 PH Parts Additively Manufactured by SLM at a Low Energy Input," *Metals*, vol. 11, no. 4, p. 588, 2021.
- [15] M. Attaran, "The rise of 3-D printing: The advantages of additive manufacturing over traditional manufacturing," *Buisness Horizons*, vol. 60, no. 5, pp. 677-688, 2017.
- [16] T. D. Ngo, A. Kashani, G. Imbalzano, K. T. Nguyen and D. Hui, "Additive manufacturing (3D printing): A review of materials, methods, applications and challenges," *Composites Part B*, vol. 143, pp. 172-196, 2018.
- [17] A. J. Pinkerton, "[Invited] Lasers in additive manufacturing," *Optics & Laser Technology*, vol. 78, pp. 25-32, 2016.
- [18] B. Van der Schueren and J. P. Kruth, "Powder deposition in selective metal powder sintering," *Rapid Prototyping Journal*, vol. 1(3), pp. 23-31, 1995.
- [19] J. Metelkova, Y. Kinds, K. Kempen, C. d. Formanoir, A. Witvrouw and B. Van Hooreweder, "On the influence of laser defocusing in Selective Laser MELting of 316L," *Additive Manufacturing*, vol. 23, pp. 161-169, 2018.
- [20] J.-P. Kruth, P. Mercelis, J. Van Vaerenbergh, L. Froyen and M. Rombouts, "Binding mechanisms in selective laser sintering and selective laser melting," *Rapid Prototyping Journal*, vol. 11, no. 1, pp. 26-36, 2005.

- [21] W. E. King, H. D. Barth, V. M. Castillo, G. F. Gallegos, J. W. Gibbs, D. E. Hahn, C. Kamath and A. M. Rubenchik, "Observation of keyhole-mode laser melting in laser powder-bed fusion additive manufacturing," *Journal of Materials Processing Technology*, vol. 214, no. 12, pp. 2915-2925, 2014.
- [22] L. C. Zhang, A. Attar, M. Calin and J. Eckert, "Review on manufacture by selective laser melting and properties of titanium based materials for biomedical applications," *Materials Technology*, vol. 31, no. 2, 2016.
- [23] Z. J. Wally, A. M. Haque, A. Feteira, F. Claeysens, R. Goodall and G. C. Reilly, "Selective laser melting processed Ti6Al4V lattices with graded porosities for dental applications," *Journal of the Mechanical Behaviour of Biomedical Materials*, vol. 90, pp. 20-29, 2019.
- [24] Y.-K. Ahn, H.-G. Kim, H.-K. Park, G.-H. Kim, K.-H. Jung, C.-W. Lee, W.-Y. Kim, S.-H. Lim and B.-S. Lee, "Mechanical and microstructural characteristics of commercial purity titanium implants fabricated by electron beam additive manufacturing," *Materials Letters*, vol. 187, pp. 64-67, 2017.
- [25] L. E. Murr, S. M. Gaytan, D. A. Ramirez, E. Martinez, J. Hernandez, K. N. Amato, P. W. Shindo, F. R. Medina and R. B. Wicker, "Metal Fabrication by Additive Manufacturing Using Laser and Electron Beam Melting Technologies," *Journal of Materials Science and Technology*, vol. 28, no. 1, pp. 1-14, 2012.
- [26] D. R. Waryoba, J. S. Keist, C. Ranger and T. A. Palmer, "Microtexture in additively manufactured Ti-6Al-4V fabricated using direct energy deposition," *Materials Science and Engineering A*, vol. 734, pp. 149-163, 2018.
- [27] N. A. Kistler, D. J. Corbin, A. R. Nassar, E. W. Reutzler and A. M. Beese, "Effect of processing conditions on the microstructure, porosity, and mechanical properties of Ti-6Al-4V repair fabricated by directed energy deposition," *Journal of Materials Processing Technology*, vol. 264, pp. 172-181, 2019.
- [28] J. Tuominen, S. Thieme, J. Nakki, S. Nowotny and P. Vuoristo, "Laser strip cladding for large area metal deposition," *Additive Manufacturing*, 2019.
- [29] Z. Wang, J. Zhang, P. Zhang, H. Zhou and T. Zhou, "Effect of the 75ferrosilicon on the laser cladding on gray cast iron," *Optics & Laser Technology*, vol. 113, pp. 64-71, 2019.
- [30] H.-J. Lee, H.-U. Kim and B.-S. Lee, "Influence of the focus offset on the defects, microstructure, and mechanical properties of Inconel 718 superalloy fabricated by electron

- beam additive manufacturing," *Journal of Alloys and Compounds*, vol. 781, pp. 842-856, 2019.
- [31] Z. C. Cordero, H. M. Meyer III, P. Nandwana and R. R. Dehoff, "Powder bed charging during electron-beam additive manufacturing," *Acta Materialia*, vol. 124, pp. 437-445, 2017.
- [32] S. Rios, P. A. Colegrove and S. W. Williams, "Metal transfer modes in plasma Wire + Arc additive mnaufacture," *Journal of Materials Processing Technology*, vol. 264, pp. 45-54, 2019.
- [33] E. Klar, P. Samal and P. Samal, *Powder Metallurgy Stainless Steels: Processing, Microstructures and Properties*, Ohio: ASM International, 2007.
- [34] K. Kassym and A. Perveen, "Atomization processes of metal powders for 3D printing," *Matraialstoday: Proceedings*, 2020.
- [35] O. Benafan , G. S. Bigelow, M. Elahinia, N. S. Moghaddam, A. Amerinatanzi, S. Saedi, G. P. Toker and H. Karaca, "Additive Manufacturing of NiTiHf High Temperature Shape Memory Alloy," *NASA*, 2017.
- [36] Z. Snow, R. Martukanitz and S. Joshi, "On the development of powder spreadability metrics and feedstock requirements for powder bed fusion additive manufacturing," *Additive Manufacturing*, vol. 28, pp. 78-86, 2019.
- [37] B. Fullenwinder, P. Kiani, J. M. Schoenung and K. Ma, "Two-stage ball milling of recycled machining chips to create an alternative feedstock powder for metal additive manufacturing," *Powder Technology*, vol. 342, pp. 562-571, 2019.
- [38] K. Ito and Y. Ichikawa, "Microstructure cntrol of cold-sprayed pure iron coatings formed using mechanically milled powder," *Surface and Coatings Technology*, vol. 357, pp. 129-139, 2019.
- [39] K. K. Koch, D. G. Morris, K. Lu and A. Inoue, "Ductility of nanostructured materials," *Materials Research Bulletin*, vol. 24, no. 2, pp. 54-58, 1999.
- [40] J. Kano and F. Saito, "Correlation of powder characteristics of talc during Planetary Ball Milling with the impact energy of the balls simulated by the Particle Element Method," *Powder Technology*, vol. 98, pp. 166-170, 1998.
- [41] J. R. Weertman, D. Farkas, K. Hemker, H. Kung, M. Mayo, R. Mitra and H. Van Swygenhoven, "Structure and mechanical behaviour of bulk nanocrystalline materials," *Materials Research Bulletin*, vol. 24, no. 2, pp. 44-53, 1999.

- [42] A. Salak, *Ferrous Powder Metallurgy*, Cambridge: Cambridge International Science Publishing, 1995.
- [43] P. C. Angelo and R. Subramanian, *Powder Metallurgy: Science, Technology and Applications*, New Delhi: PHI Learning Private Limited, 2008.
- [44] G. S. Upadhyaya, *Powder Metallurgy Technology*, Cambridge: Cambridge International Science Publishing, 2002.
- [45] T. DebRoy, H. L. Wei, J. S. Zuback, T. Mukherjee, J. W. Elmer, J. O. Milewski, A. Wilson-Heid, A. De and W. Zhang, "Additive manufacturing of metallic components - Process, structure and properties," *Progress in Materials Science*, pp. 112-224, 2018.
- [46] N. Shamsaei, A. Yadollahi, L. Bian and S. M. Thompson, "An overview of Direct Laser Deposition for additive manufacturing Part II: Mechanical behavior, process parameter optimization and control," *Additive Manufacturing*, vol. 8, pp. 12-35, 2015.
- [47] M. Guo, D. Gu, L. Xi, H. Zhang, J. Yang and R. Wang, "Selective laser melting additive manufacturing of pure tungsten: Role of volumetric energy density on densification, microstructure and mechanical properties," *International Journal of Refractory Metals and Hard Materials*, vol. 84, 2019.
- [48] E. B. Fonseca, A. H. G. Gabriel, L. C. Araujo, P. L. L. Santos, K. N. Campo and E. S. N. Lopes, "assessment of laser power and scan speed influence on microstructural features and consolidation of AISI H13 tool steel processed by additive manufacturing," *Additive Manufacturing*, vol. 34, 2020.
- [49] W. Di, Y. Yongqiang, S. Xubin and C. Yonghua, "Study on energy input and its influences on single-track, multi-track, and multi-layer in SLM," *The International Journal of Advanced Manufacturing Technology*, vol. 58, pp. 1189-1199, 2012.
- [50] X. Sun, D. Liu, W. Zhou, N. Nomura, Y. Tsusumi and T. Hanawa, "Effects of process parameters on mechanical properties of additively manufactured Zr-1Mo alloy builds," *Journal of Mechanical Behaviour of Biomedical Materials*, vol. 104, 2020.
- [51] U. S. Bertoli, A. J. Wolfer, M. J. Matthews, J.-P. R. Delplanque and J. M. Schoenung, "On the limitations of Volumetric Energy Density as a design parameter for Selective Laser Melting," *Materials & Design*, vol. 113, pp. 331-340, 2017.
- [52] T. W. Eagar and N. S. Tsai, "Temperature Fields Produced by Traveling Distributed Heat Sources," *Welding Journal*, vol. 62, pp. 346-355, 1983.

- [53] G. Tapia, A. H. Elwany and H. Sang, "Prediction of porosity in metal-based additive manufacturing using spatial Gaussian process models," *Additive Manufacturing*, vol. 12, pp. 282-290, 2016.
- [54] S. m. Ahmadi, R. K. Hedayati, Y. L. Leeftang and A. A. Zadpoor, "Effects of laser processing parameters on the mechanical properties, topology, and microstructure of additively manufactured porous metallic biomaterials: A vector-based approach," *Materials & Design*, vol. 134, pp. 234-243, 2017.
- [55] A. Suzuki, R. Nishida, N. Takata, M. Kobashi and M. Kato, "Design of laser parameters for selectively laser melted maraging steel based on deposited energy density," *Additive Manufacturing*, vol. 28, pp. 160-168, 2019.
- [56] H. D. Carlton, A. Haboub, G. F. Gallegos, D. Y. Parkinson and A. A. MacDowell, "Damage evolution and failure mechanisms in additively manufactured stainless steel," *Materials Science & Engineering A*, vol. 651, pp. 406-414, 2016.
- [57] J. A. Cherry, H. M. Davies, S. Mehmood, N. P. Lavery, S. G. R. Brown and J. Sienz, "Investigation into the effect of process parameters on microstructural and physical properties of 316L stainless steel parts by selective laser melting," *International Journal of Advanced Manufacturing Technology*, vol. 76, pp. 869-879, 2015.
- [58] E. Yasa and J.-P. Kruth, "Microstructural investigation of Selective Laser Melting 316L stainless steel parts exposed to laser re-melting," *Procedia Engineering*, vol. 19, pp. 389-395, 2011.
- [59] T. Heeling, M. Cloots and K. Wegener, "Melt pool simulation for the evaluation of process parameters in selective laser melting," *Additive Manufacturing*, vol. 14, pp. 116-125, 2017.
- [60] J. L. Bartlett, F. M. Heim, Y. V. Murty and X. Li, "In Situ defect detection in selective laser melting via full-field infrared thermography," *Additive Manufacturing*, vol. 24, pp. 595-605, 2018.
- [61] N. K. Tolochko, S. E. Mozzharov, I. A. Yadroitsev, T. Laoui, L. Froyen, V. Titov and M. B. Ignatiev, "Balling processes during selective laser treatment of powders," *Rapid Prototyping*, vol. 10, no. 2, 2004.
- [62] Y.-D. Qiu, J.-M. Wu, A.-N. Chen, P. Chen, Y. Yang, R.-Z. Liu, G. Chen, S. Chen, Y.-S. Shi, Y.-S. Shi and C.-H. Li, "Balling phenomenon and cracks in alumina ceramics

- prepared by direct selective laser melting assisted with pressure treatment," *Ceramics International*, vol. 46, no. 9, pp. 13854-13861, 2020.
- [63] A. Yan, Z. Wang, T. Yang, Y. Wang and Z. Ma, "Microstructure, thermal physical property and surface morphology of W-Cu composite fabricated via selective laser melting," *Materials and Design*, vol. 109, pp. 79-87, 2016.
- [64] K. Wei, M. Gao, Z. Wang and X. Zeng, "Effect of energy input on formability and mechanical properties of selective laser melted AZ91D magnesium alloy," *Materials Science and Engineering: A*, vol. 611, pp. 212-222, 2014.
- [65] H. Gong, K. Rafi, H. Gu, T. Starr and B. Stucker, "Analysis of defect generation in Ti-6Al-4V parts made using powder bed fusion additive manufacturing processes," *Additive Manufacturing*, Vols. 1-4, pp. 87-98, 2014.
- [66] B. Zhang, Y. Li and Q. Bai, "Defect Formation Mechanisms in Selective Laser Melting: A Review," *Chinese Journal of Mechanical Engineering*, vol. 30, pp. 515-527, 2017.
- [67] M. Tang, P. C. Pistorius and J. L. Beuth, "Prediction of lack-of-fusion porosity for powder bed fusion," *Additive Manufacturing*, vol. 14, pp. 39-48, 2017.
- [68] S. Coeck, M. Bisht, J. Plas and F. Verbist, "Prediction of lack of fusion porosity in selective laser melting based melt pool monitoring data," *Additive Manufacturing*, vol. 25, pp. 347-356, 2019.
- [69] Y. N. Hu, S. C. Wu, P. J. Withers, J. Zhang, H. Y. X. Bao, Y. N. Fu and G. Z. Kang, "The effect of manufacturing defects on the fatigue life of selective laser melted Ti-6Al-4V structures," *Materials & Design*, vol. 192, 2020.
- [70] G. Kasperovich, J. Haubrich, J. Gussone and G. Requena, "Correlation between porosity and processing parameters in TiAl6V4 produced by selective laser melting," *Materials & Design*, vol. 105, pp. 160-170, 2016.
- [71] K. V. Yang, P. Rometsch, T. Jarvis, J. Rao, S. Cao, C. Davies and X. Wu, "Porosity formation mechanisms and fatigue in Al-Si-Mg alloys made by selective laser melting," *Materials Science and Engineering: A*, vol. 712, pp. 166-174, 2018.
- [72] C. Tang, J. L. Tan and C. H. Wong, "A numerical investigation on the physical mechanisms of single track defects in selective laser melting," *International Journal of Heat and Mass Transfer*, vol. 126, pp. 957-968, 2018.
- [73] K. Q. Le, C. Tang and C. H. Wong, "On the study of keyhole-mode melting in selective laser melting process," *International Journal of Thermal Sciences*, vol. 145, 2019.

- [74] W. E. King, H. D. Barth, V. M. Castillo, G. F. Gallegos, J. W. Gibbs, D. E. Hahn, C. Kamath and A. M. Rubenchik, "Observation of keyhole-mode laser melting in laser powder bed fusion additive manufacturing," *Journal of Materials Processing Technology*, vol. 214, pp. 2915-2925, 2014.
- [75] N. T. Aboulkhair, I. Maskery, C. Tuck, I. Ashcroft and N. M. Everitt, "On the formation of AISi10Mg single tracks and layers in selective laser melting: Microstructure and nano-mechanical properties," *Journal of Materials Processing Technology*, vol. 230, pp. 88-98, 2016.
- [76] T. Simm, L. Sun, S. McAdam, P. Hill, M. Rawson and K. Perkins, "The Influence of Lath, Block and Prior Austenite Grain (PAG) Size on the Tensile, Creep and Fatigue Properties of Novel Maraging Steel," *Materials*, vol. 10, p. 730, 2017.
- [77] H. Asgari and M. Mohammadi, "Microstructure and mechanical properties of stainless steel CX manufactured by Direct Metal Laser Sintering," *Materials Science and Engineering: A*, vol. 709, pp. 82-89, 2018.
- [78] A. Shahriari, L. Khaskar, A. Nasiri, A. Hadadzadeh, B. Shalchi Amirkhiz and M. Mohammadi, "Microstructure and corrosion behaviour of a novel additively manufactured maraging stainless steel," *Electrochimica Acta*, vol. 339, 2020.
- [79] S. Takaki, K. Fukunaga, J. Syarif and T. Tsuchiyama, "Effect of Grain Refinement on Thermal Stability of Metastable Austenitic Steel," *Materials Transactions*, vol. 45, no. 7, pp. 2245-2251, 2004.
- [80] H. Khalid Rafi, D. Pal, T. L. Starr and B. E. Stucker, "Microstructure and Mechanical Behaviour of 17-4 Precipitation Hardenable Steel Processed by Selective Laser Melting," *Journal of Materials Engineering and Performance*, vol. 23, pp. 4421-4428, 2014.
- [81] C. Tan, K. Zhou, W. Ma, P. Zhang, M. Liu and T. Kuang, "Microstructural evolution, nanoprecipitation behavior and mechanical properties of selective laser melted high-performance grade 300 maraging steel," *Materials & Design*, vol. 134, pp. 23-34, 2017.
- [82] N. Senaei and A. Fatemi, "Analysis of the effect of surface roughness on fatigue performance of powder bed fusion additive manufactured metals," *Theoretical and applied Fracture MEchanics*, vol. 108, 2020.
- [83] ConceptLaser, "CL91-RW Stainless hot-work steel".

- [84] E. Cyr, H. Asgari, S. Shamsdini, M. Purdy, K. Hosseinkhani and M. Mohammadi, "Fracture behaviour of additively manufactured MS1-H13 hybrid hard steels," *Materials Letters*, vol. 212, pp. 174-177, 2018.
- [85] S. Bai, N. Perevoshchikova, Y. Sha and X. Wu, "The effects of Selective Laser Melting Process Parameters on Relative Density of the AlSi10Mg Parts and Suitable Procedures of the Archimedes Method," *Applied Sciences*, 2019.
- [86] S. L. Sing, F. E. Wiria and W. Y. Yeoung, "Selective laser melting of titanium alloy with 50 wt% tantalum: Effect of laser process parameters on part quality," *International Journal of Refractory Metals and Hard Materials*, vol. 77, pp. 120-127, 2018.
- [87] T. Qi, H. Zhu, H. Zhang, J. Yin, L. Ke and X. Zeng, "Selective laser melting of Al7050 powder: Melting mode transition and comparison of the characteristics between the keyhole and conduction mode," *Materials & Design*, vol. 135, pp. 257-266, 2017.
- [88] S. V. Adjamsky, Y. V. Tkachev and G. A. Kononenko, "Effect of Defective Laser Melting Parameters on the Melt Pool Formed by Single Track of Heat-Resistant Inconel 718 Nickel alloy," *Powder Metallurgy and Metal Ceramics*, no. 101, pp. 592-600, 2021.
- [89] O. Andreau, I. Koutiri, P. Peyre, J.-D. Penot, N. Saintier, E. Pessard, T. De Terris, C. Dupuy and T. Baudin, "Texture control of 316L parts by modulation of the melt pool morphology in selective laser melting," *Journal of Materials Processing Technology*, vol. 264, pp. 21-31, 2019.
- [90] C. Kusuma, S. H. Ahmed, A. Mian and R. Srinivasan, "Effect of Laser Power and Scan Speed on Melt Pool Characteristics of Commercially Pure titanium (CP-Ti)," *Journal of Materials Engineering and Performance*, vol. 26, pp. 3560-3568, 2017.
- [91] H. Choo, K.-I. Sham, J. Bohling, A. Ngo, X. Xiao, Y. Ren, P. J. Depond, M. J. Matthews and E. Garlea, "Effect of laser power on defect, texture, and microstructure of a laser powder bed fusion processed 316L stainless steel," *Materials & Design*, vol. 164, 2019.
- [92] H. Zhao, W. Niu and B. Zhang, "Modelling of keyhole dynamics and porosity formation considering the adaptive keyhole shape and three-phase coupling during deep-penetration laser welding," *Journal of Applied Physics*, vol. 44, no. 48, p. 485302, 2011.
- [93] X. Zhang, W. Chen and P. Jiang, "Modeling and application of plasma charge current in penetration laser welding," *Journal of Applied Physics*, vol. 93, no. 11, pp. 8842-8847, 2003.

- [94] L. Dowling, J. Kennedy, S. O'Shaughnessy and D. Trimble, "A review of critical repeatability and reproducibility issues in powder bed fusion," *Materials & Design*, vol. 186, 2020.
- [95] M. Yakout, M. A. Elbestawi and S. C. Veldhuis, "Density and mechanical properties in selective laser melting of Invar 36 and stainless steel 316L," *Journal of Materials Processing Technology*, vol. 266, pp. 397-420, 2019.
- [96] Y. Wang, L. Luo, T. Liu, B. Wang, L. Luo, J. Zhao, L. Wang, Y. Su, J. Guo and H. Fu, "Tuning process parameters to optimize microstructure and mechanical properties of novel maraging steel fabricated by selective laser melting," *Materials Science and Engineering: A*, vol. 823, 2021.
- [97] ConceptLaser, "CL 50WS Maraging Steel".
- [98] X. C. Wang and J. P. Kruth, "ENERGY ABSORPTION AND PENETRATION IN SELECTIVE LASER SINTERING: A RAY TRACING MODEL," *Proceedings of the International Conference on Mathematical Modelling and Simulation of Metal Technologies*, pp. 673-683, 2000.
- [99] Y. L. Kuo, S. Horikawa and K. Kakehi, "Effects of build direction and heat treatment on creep properties of Ni-base superalloy built up by additive manufacturing," *Scripta Materialia*, vol. 129, pp. 74-78, 2017.
- [100] A. T. Sidambe, Y. Tian, P. B. Prangnell and P. Fox, "Effect of processing parameters on the densification, microstructure and crystallographic texture during the laser powder bed fusion of pure tungsten," *International Journal of Refractory Metal and Hard Materials*, vol. 78, pp. 254-263, 2019.
- [101] H. Yu, F. Li and X. Zeng, "Fatigue performances of selective laser melted Ti-6Al-4V alloy: Influence of surface finishing, hot isostatic pressing and heat treatments," *International Journal of Fatigue*, vol. 120, pp. 175-183, 2019.
- [102] B. Ferrar, L. Mullen, R. Stamp and C. J. Sutcliffe, "Gas flow effects on selective laser melting (SLM) manufacturing performance," *Journal of Materials Processing Technology*, vol. 212, pp. 355-364, 2012.
- [103] M. Mohammadi and H. Asgari, "Achieving low surface roughness AlSi10Mg_200C parts using direct metal laser sintering," *Additive Manufacturing*, vol. 20, pp. 23-32, 2018.
- [104] K. Kapoor, Y. S. J. Yoo, T. A. Book, J. P. Kacher and M. D. Sangid, "Incorporating grain-level residual stresses and validating a crystal plasticity model of a two-phase Ti-6Al-4V

alloy produced via additive manufacturing," *Journal of the Mechanics and Physics of Solids*, vol. 121, pp. 447-462, 2018.

Curriculum Vitae

Candidate's full name: Mackenzie Purdy

Universities attended:

University of New Brunswick, Fredericton, New Brunswick, Canada (2013-2018):

B.Sc. Mechanical Engineering

Publications and Conference Presentations:

Cyr, E., Asgari, H., Shamsdini, S., Purdy, M., Hosseinkhani, K., & Mohammadi, M. (2018).” *Fracture behaviour of additively manufactured MS1-H13 hybrid hard steels,*” *Materials Letters*, 212, 174-177.